

1 **Enhanced daytime secondary aerosol formation driven by**
2 **gas-particle partitioning in downwind urban plumes**

3 Mingfu Cai^{1,2,3}, Chenshuo Ye⁴, Bin Yuan^{2,3*}, Shan Huang^{2,3}, E Zheng^{2,3}, Suxia Yang⁵,
4 Zelong Wang^{2,3}, Yi Lin^{2,3}, Tiange Li^{2,3}, Weiwei Hu⁶, Wei Chen⁶, Qicong Song^{2,3}, Wei
5 Li^{2,3}, Yuwen Peng^{2,3}, Baoling Liang⁷, Qibin Sun⁷, Jun Zhao⁷, Duohong Chen⁸, Jiaren
6 Sun¹, Zhiyong Yang⁹, Min Shao^{2,3}

7 ¹Guangdong Province Engineering Laboratory for Air Pollution Control, Guangdong Provincial Key
8 Laboratory of Water and Air Pollution Control, South China Institute of Environmental Sciences, MEE,
9 Guangzhou 510655, China

10 ²Institute for Environmental and Climate Research, Jinan University, Guangzhou 51143, China

11 ³Guangdong-Hongkong-Macau Joint Laboratory of Collaborative Innovation for Environmental
12 Quality, Jinan University, Guangzhou 510632, China

13 ⁴ Guangdong Provincial Academy of Environmental Science, Guangzhou, 510045, China

14 ⁵ Guangzhou Research Institute of Environment Protection Co.,Ltd, Guangzhou 510620, China

15 ⁶State Key Laboratory of Organic Geochemistry and Guangdong Key Laboratory of Environmental
16 Protection and Resources Utilization, Guangzhou Institute of Geochemistry, Chinese Academy of
17 Sciences, Guangzhou 510640, China

18 ⁷School of Atmospheric Sciences, Guangdong Province Key Laboratory for Climate Change and
19 Natural Disaster Studies, and Institute of Earth Climate and Environment System, Sun Yat-sen
20 University, Zhuhai 519082, China

21 ⁸Guangdong Environmental Monitoring Center, Guangzhou 510308, China

22 ⁹Guangzhou Huangpu District Meteorological Bureau, Guangzhou 510530, China

23
24 **Corresponding authors: Bin Yuan (byuan@jnu.edu.cn)*
25

26 **Abstract.**

27 Anthropogenic emissions from city clusters can significantly enhance secondary organic
28 aerosol (SOA) formation in the downwind regions, while the mechanism is poorly understood. To
29 investigate the effect of pollutants within urban plumes on organic aerosol (OA) evolution, a field
30 campaign was conducted at a downwind site of the Pearl River Delta region of China in the fall of
31 2019. A time-of-flight chemical ionization mass spectrometer coupled with a Filter Inlet for Gases
32 and Aerosol (FIGAERO-CIMS) was used to probe the gas- and particle-phase molecular
33 composition and thermograms of organic compounds. For air masses influenced by urban pollution,
34 strong daytime SOA formation through gas-particle partitioning was observed, resulting in higher
35 OA volatility. The obvious SOA enhancement was mainly attributed to the gas-particle partitioning
36 of high volatility (SVOC+IVOC+VOC, $C^* > 0.3 \mu\text{g m}^{-3}$) organic vapors. Using the equilibrium
37 equation could underestimate the contribution of high volatility organic vapors, since the volatility
38 of these species in the particle-phase was lower than that in the gas-phase. We speculated that the
39 elevated NO_x concentration could suppress the formation of highly oxidized products, resulting in
40 a smooth increase of low volatility (ELVOC+LVOC, $C^* \leq 0.3 \mu\text{g m}^{-3}$) organic vapors. Evidences
41 showed that urban pollutants (NO_x and VOCs) could enhance the oxidizing capacity, while the
42 elevated VOCs were mainly responsible for promoting daytime SOA formation by increasing the
43 RO_2 production rate. Our results highlight the important role of urban anthropogenic pollutants in
44 SOA control in the suburban region.

45 **1. Introduction**

46 As a major concern of air pollution, aerosol particles are known to have significant impacts on
47 public health and climate (Apte et al., 2018; Arias et al., In Press). Primary particulate matter (PM)
48 in China has shown a remarkable reduction since 2013, owing to strictly clean air policies
49 implemented by the Chinese government (Zhang et al., 2019). Despite the effective reduction of
50 primary emissions in the past ten years, secondary organic aerosol (SOA) remains at high levels and
51 is mainly responsible for the haze development in China(Huang et al., 2014). SOA is thought to be
52 formed through the oxidation of volatile organic compounds (VOCs) and atmospheric aging
53 processes of primary organic aerosol (POA). However, models are especially challenged in
54 reproducing SOA concentration and properties, since the formation mechanisms and gas precursors
55 of SOA remain poorly characterized(Hodzic et al., 2010).

56 Gas-particle partitioning of organic vapors is found to be the important formation pathway of
57 SOA the worldwide(Nie et al., 2022; Hallquist et al., 2009; Lanzafame et al., 2021). Nie et al. (2022)
58 suggested that the contribution of the condensation of organic vapors to the SOA mass growth
59 ranged from about 38%-71% in China megacities. Photochemical produced SOA via gas phase
60 chemistry is usually related to a higher volatility and a lower oxidation degree than that formed in
61 the aqueous phase (Ervens et al., 2011; Saha et al., 2017). The condensation processes of organic
62 vapors are determined by their volatility, which is closely related to oxidation state, functional
63 groups, and the number of atomic carbons. Laboratory studies revealed that high nitrogen oxides
64 (NO_x) concentration can suppress the production of molecules with high oxidation degree by
65 inhibiting autoxidation(Rissanen, 2018; Peng et al., 2019), which is considered to be an important
66 pathway of low volatility vapor formation(Praske et al., 2018). Such compounds have been shown
67 to play a vital role in the SOA formation and growth of newly formed particles(Mutzel et al., 2015;
68 Bianchi et al., 2019; Mohr et al., 2019). On the other hand, it is shown that the increase of oxidant
69 owing to elevated NO_x concentration can offset the decrease of autoxidation efficiency, leading to a
70 higher production of oxygenated organic vapors(Pye et al., 2019), highlighting the complexity of
71 SOA formation. However, the lack of a molecular dataset of SOA and gas precursors hinders the
72 understanding of the SOA formation mechanism.

73 Recently, a chemical ionization time-of-flight mass spectrometer coupled with a Filter Inter for

74 Gases and AEROSols (FIGAERO-CIMS) has been employed to measure gas- and particle-phase
75 oxygenated organic compounds worldwide (Chen et al., 2020; Buchholz et al., 2020; Masoud et
76 al., 2022). Using a FIGAERO-CIMS, Cai et al. (2023) showed that heterogeneous reaction might
77 have an important role in the secondary formation of particle-phase oxidized organic nitrogen. The
78 volatility of OA can provide information about the formation and aging processes of OA, given that
79 it is strongly affected by chemical composition. In past decades, a thermodenuder (TD) coupled
80 with aerosol detection instruments (e.g. aerosol mass spectrometer and condensation particle
81 counter) was widely used in the estimation of OA volatility (Philippin et al., 2004; Lee et al., 2010).
82 Cai et al. (2022) found that the OA volatility was higher at a particle size range of 30 to 200 nm
83 during daytime, suggesting that the SOA formation through gas-particle partitioning could generally
84 occur at all particle sizes. However, this method failed to provide the volatility information of
85 different molecules of OA. In recent years, the FIGAERO-CIMS was developed to characterize the
86 volatility of oxygenated organic molecules in the particle phase. (Ren et al., 2022; Ylisirniö et al.,
87 2020). Wang and Hildebrandt Ruiz (2018) showed that the thermal desorption products of SOA can
88 be separated into different groups on a two-dimensional thermogram measured by the FIGAERO-
89 CIMS. Ren et al. (2022) investigated the relationship between the molecular formulae of OA
90 components and their volatilities and suggested that the volatility of OA compounds was strongly
91 affected by O to C ratio. These results provide valuable insights into the SOA formation mechanisms.
92 However, as yet few FIGAERO-CIMS field studies are available in the literature in China (Ye et al.,
93 2021; Salvador et al., 2021), especially in urban downwind areas.

94 Observational studies have demonstrated that anthropogenic emissions can significantly affect
95 SOA formation in the downwind region. Fry et al. (2018) observed an enhancement of organic
96 nitrate aerosol formed through NO_3 +isoprene in power plant plume during nighttime, which was
97 mainly attributed to NO_x emissions from the power plant. The results from Liu et al. (2018)
98 suggested that the OH concentrations increased by at least 250% under polluted conditions, which
99 might promote the daytime SOA formation. A field measurement in the Amazon forest by De Sá et
100 al. (2018) showed that the enhancement of OA (about 30-171%) in urban plumes was mainly
101 contributed by SOA. A recent study found that anthropogenic emission of NO_x from urban could
102 enhance oxidant concentration, thereby promoting daytime SOA formation (Shrivastava et al., 2019).

103 In this study, we investigate the SOA formation through photochemical reactions at a typical

104 downwind site in the Pearl River Delta region (PRD) using a FIGAERO-CIMS along with a suite
105 of other online instruments. The volatility of OA and its relationship with identified OA sources
106 during long-range transport, urban air masses, and coastal air masses periods are discussed. The
107 formation mechanisms of daytime SOA formation within the urban plume are investigated based on
108 online measurements of gas- and particle-phase organic compounds, gaseous pollutants, and aerosol
109 physicochemical properties. The impact of urban pollutants on SOA formation will be discussed.

110 **2. Measurement and Method**

111 **2.1 Field measurement**

112 The campaign was conducted at the Heshan supersite in the PRD region during the fall of 2019
113 (29th September to 17th November 2019). The Heshan Supersite, surrounded by farms and villages,
114 is located (at 22°42'39. 1"N, 112°55'35.9"E, with an altitude of about 40 m) at southwest of the
115 PRD region and about 70 km southwest of Guangzhou city (Fig. S1). During the measurement, the
116 sampling site is mainly influenced by the air masses from the center of the PRD region (Fig. S2a).
117 All instruments were placed in an air-conditioned room on the top floor of the supersite. A detailed
118 description of the site and experimental setup can be found in Cai et al. (2021).

119 **2.2 Instrumentation**

120 **2.2.1 FIGAERO-CIMS**

121 A FIGAERO-CIMS coupled with an X-ray source was employed to measure organic
122 compounds in the gas- and particle-phase using I⁻ as the chemical ionization reagent. The particle
123 sampling inlet of the FIGAERO-CIMS was equipped with a PM_{2.5} cyclone and a Nafion dryer
124 (model PD-07018T-12MSS, Perma Pure, Inc., USA). The principle of the instrument can be found
125 in Lopez-Hilfiker et al. (2014) and Le Breton et al. (2018). In general, the operation settings and
126 data processing were the same as Cai et al. (2023) and Ye et al. (2021). Here, only a brief description
127 relevant to the measurement is given. The instrument was worked in a cycle pattern of 1 hour, with
128 24 minutes of gas-phase measurements and particle collection (sampling mode), followed by a 36-
129 minutes particle-phase analysis (desorption mode). In the sampling mode, ambient gas was

130 measured in the first 21 minutes, followed by a 3-min zero air background. At the same time,
131 ambient particles were collected on a PTFE membrane filter. In the desorption mode, the collected
132 particles were desorbed by heated N₂. The temperature of the N₂ was linearly ramped from indoor
133 temperature (~25°C) to ~175 °C in 12 minutes and held for 24 minutes. The data processing steps
134 in this campaign were the same as Ye et al. (2021). A few chemicals were calibrated before and after
135 the measurement. For uncalibrated species, a voltage scanning method was employed to obtain their
136 sensitivities (referred to as semi-quantified species) (Ye et al., 2021; Iyer et al., 2016; Lopez-Hilfiker
137 et al., 2016).

138 2.2.2 SP-AMS

139 The PM₁ chemical composition was measured by a soot particle aerosol mass spectrometer
140 (SP-AMS, Aerodyne Research, Inc., USA). The details of the operation and data analysis can be
141 found in Kuang et al. (2021). Source apportionment was performed for organic aerosols in the bulk
142 PM₁ using positive matrix factorization (PMF). The organic aerosol could be divided into six
143 components, including two primary OA factors and four secondary OA factors. The mass spectral
144 profiles of six OA factors are shown in Figure S3. The time series and diurnal variation of these
145 factors are presented in Figure S4.

146 The primary OA factors include hydrocarbon-like OA (HOA), mainly contributed by traffic
147 and cooking emissions and biomass burning OA (BBOA) originating from biomass burning
148 combustion. The HOA was identified by hydrocarbon ions C_xH_y⁺. Owing to the prominent
149 hydrocarbon ions and low O:C value (0.10), HOA could be attributed to primary emission from
150 cooking and traffic. The BBOA was recognized by the markers C₂H₄O₂⁺ (m/z 60.022, 0.5%) and
151 C₃H₅O₂⁺ (m/z 73.029, 0.4%), which are considered tracers for biomass burning OA (Ng et al., 2011).

152 The SOA factors include biomass burning SOA (BBSOA) likely formed from oxidation of
153 biomass burning emission, less oxygenated OA (LOOA) provided by strong daytime photochemical
154 formation, more oxygenated OA (MOOA) related to regional transport, and nighttime-formed OA
155 (Night-OA) contributed by secondary formation during nighttime. The BBSOA was likely formed
156 through oxidation of biomass burning precursors, which was supported by the evening peak at about
157 19:00 LT (Fig. S4). BBSOA showed a similar variation trend with C₆H₂NO₄⁺, which might be

158 contributed by oxidation of gaseous precursors from biomass burning emissions (Wang et al., 2019;
159 Bertrand et al., 2018). The significant afternoon peak of LOOA indicates its formation through
160 photochemical reactions, which will be discussed in detail in section 3.1. The negligible diurnal
161 variation and the highest O:C value (1.0) of MOOA suggested that it could be aged OA resulting
162 from long-range transport. Night-OA was formed through NO₃ nighttime chemistry, supported by
163 a pronounced evening elevation and positive correlation with nitrate (R=0.67). The detailed
164 determination of PMF factors has been found in Kuang et al. (2021) and Luo et al. (2022).

165 **2.2.3 Particle number size distribution measurements**

166 Particle number size distribution in a size range of 1 nm - 10 μm was measured by a diethylene
167 glycol scanning mobility particle sizer (DEG-SMPS, model 3938E77, TSI Inc., USA), a SMPS
168 (model 3938L75, TSI Inc., USA), and an aerodynamic particle sizer (APS, model 3321, TSI Inc.,
169 USA). All sample particles first passed through a Nafion dryer (Model MD-700, Perma Pure Inc.,
170 USA) to reduce relative humidity (RH) lower than 30%. A detailed description of these instruments
171 can be found in Cai et al. (2021).

172 **2.2.4 Other parameters**

173 The non-methane hydrocarbons (NMHC) were measured by an online GC-MS-FID (Wuhan
174 Tianhong Co., Ltd, China). The concentration of oxygenated VOCs, including formaldehyde
175 (HCHO) and acetaldehyde (CH₃CHO), were measured using high-resolution proton transfer
176 reaction time-of-flight mass spectrometry (PTR-ToF-MS, Ionicon Analytik, Austria). HONO was
177 detected by the gas and aerosol collector (GAC) instrument (Dong et al., 2012). Trace gases,
178 including O₃, NO_x, and CO, were measured by gas analyzers (model 49i, 42i, and 48i, Thermo
179 Scientific, US). Meteorological parameters (i.e., wind speed, wind direction, and temperature) were
180 measured by a weather station (Vantage Pro 2, Davis Instruments Co., US).

181 **2.3 Methodology**

182 **2.3.1 Estimation of the volatility of particle- and gas-phase organic compounds**

183 During the heating processes, the FIGAERO-CIMS simultaneously measured the desorbing

184 compounds of the collected particles. Thus, the volatility information of particles can be obtained
185 by investigating the relationship between the measured signals and desorption temperature. The
186 temperature of the peak desorption signal (T_{max}) has a nearly linear relationship with the natural
187 logarithm of saturation vapor pressure (P_{sat}) of the respective compound (Lopez-Hilfiker et al.,
188 2014):

$$189 \quad \ln(P_{sat}) = aT_{max} + b \quad (1)$$

190 where a and b are fitting coefficients. Thus, saturation vapor concentration (C^* , $\mu\text{g m}^{-3}$) can be
191 obtained:

$$192 \quad C^* = \frac{P_{sat}M_w}{RT} 10^6 \quad (2)$$

193 where M_w is the molecular weight of the compound (determined by the FIGAERO-CIMS), R is the
194 universal gas constant ($8.314 \text{ J mol}^{-1} \text{ K}^{-1}$), and T is the thermodynamic temperature in kelvin (298.15
195 K).

196 We used a series of polyethylene glycol (PEG 5-8) compounds to calibrate the T_{max} and
197 obtained the fitting parameters a and b . The PEG standards were prepared in a mixture of
198 acetonitrile and then atomized with a homemade atomizer. The atomized particles are classified by
199 a differential mobility analyzer (DMA, model 3081 L, TSI Inc., USA) at two diameters (100 nm
200 and 200 nm). The selected particles were then split into two paths: one to a condensation particle
201 counter (CPC, model 3775, TSI Inc., USA) for measuring the particle concentration and another
202 one to the particle inlet of the FIGAERO-CIMS. The collected concentration can be calculated based
203 on the selected particle diameter, particle number concentration, flow rate of the particle inlet of
204 FIGAERO-CIMS, and collection time. The calibration results and corresponding fitting parameters
205 can be found in Fig. S5 and Table. S1. Note that the T_{max} can vary with mass loading, and it is
206 necessary to consider this for estimation the relationship between T_{max} and C^* (Wang and
207 Hildebrandt Ruiz, 2018). Our calibration results demonstrated that the correlation between T_{max}
208 shift and mass loading was not linear, which may be attributed to matrix or saturation effects (Huang
209 et al., 2018). During the measurement, the collected mass loading centered at about 620 ng and the
210 particle volume size distribution (PVSD) centered at about 400 nm (Fig. S6). Thus, the fitting
211 parameters ($a=-0.206$ and $a=3.732$) of the calibration experiment with a diameter of 200 nm and
212 mass loading of 407 ng were adopted in the C^* calculation, since the mass loading and diameter are

213 the closest to the ambient samples.

214 For gas-phase organic compounds (organic vapors), we first divided them into two groups
215 based on their oxidation pathways (multi-generation OH oxidation and autoxidation, solid line in
216 Fig. S7) and then used different parameters in their volatility estimation. The classification of
217 pathways was based on the molecular characteristics of oxidation products of aromatics and
218 monoterpene, respectively (Wang et al., 2020). In general, their saturation vapor concentration (C^* ,
219 at 300 K) can be estimated as follows:

$$220 \quad \log_{10}(C^*(300K)) = (25 - n_C) \cdot b_C - (n_O - 3n_N) \cdot b_O - \frac{2(n_O - 3n_N)n_C}{(n_C + n_O - 3n_N)} \cdot b_{CO} - n_N \cdot b_N \quad (3)$$

221 where n_C , n_O , and n_N are the numbers of carbon, oxygen, and nitrogen atoms in each compound.
222 For oxidation products formed from multi-generation OH oxidation (aging) pathway, the volatility
223 parameters b_C , b_O , b_{CO} , and b_N were assumed to be 0.475, 2.3, -0.3, and 2.5, respectively (Donahue
224 et al., 2011). For oxidation products formed from autoxidation pathway, the modified
225 parameterization is used, with $b_C=0.475$, $b_O=0.2$, $b_{CO}=0.9$, and $b_N=2.5$ (Bianchi et al., 2019). It
226 should be noted that this method can only roughly distinguish the formation pathways of ambient
227 organic vapors, since it is based on the oxidation products of specific species in a laboratory study.

228 2.3.2 Calculation of oxidation state (\overline{OS}_C) of $C_xH_yO_z$ and $C_xH_yN_{1,2}O_z$ compounds

229 For $C_xH_yO_z$ compounds, the \overline{OS}_C can be estimated as:

$$230 \quad \overline{OS}_C = 2 \times \frac{O}{C} - \frac{H}{C} \quad (4)$$

231 For $C_xH_yN_{1,2}O_z$ compounds, the \overline{OS}_C can be calculated from following equation:

$$232 \quad \overline{OS}_C = 2 \times \frac{O}{C} - \frac{H}{C} - x \times \frac{N}{C} \quad (5)$$

233 where x is the valence state of N atoms, which is dependent on functional groups. Several
234 assumptions were adopted to classify them. (1)N-containing functional groups were nitro (-NO₂,
235 $x=+3$) or nitrate (-NO₃, $x=+5$) in our measurement; (2)N-containing aromatics contain nitro
236 moieties while N-containing aliphatic hydrocarbons contain nitrate moieties; (3)N-containing
237 aromatics have 6-9 carbon atoms and fewer hydrogen atoms than aliphatic hydrocarbons with the
238 same number of carbon atoms.

239 2.3.3 Estimation of condensation sink

240 The condensation sink (CS) represents the condensing vapor captured by pre-existing particles
241 and can be calculated from the following equation:

$$242 \quad CS = 2\pi D \sum_{D_p} \beta_{m,D_p} D_p N_{D_p} \quad (6)$$

243 where D is the diffusion coefficient of the H_2SO_4 vapor ($0.8 \times 10^{-5} \text{ m}^2 \text{ s}^{-1}$), β_{m,D_p} is the
244 transitional regime correction factor which can be calculated from the Knudsen number (Fuchs and
245 Sutugin, 1971), and N_{D_p} represents the particle number concentration at D_p .

246 2.3.4 Estimation of OA contributed by high volatility organic vapors

247 Organic vapors with higher volatility (SVOC+IVOC+VOC, $C^* > 0.3 \mu\text{g m}^{-3}$) can easily reach
248 an equilibrium between the gas and particle phase. Thus, the contribution of high volatility organic
249 vapors to OA concentration (OA_{HVgas}) through gas-particle partitioning can be estimated as
250 following:

$$251 \quad OA_{HVgas} = \sum_i C_{i,g} f_i \quad (7)$$

252 where $C_{i,g}$ is the gas-phase concentration of species i . f_i is the fraction of species i in the particle
253 phase and is defined as:

$$254 \quad f_i = \frac{C_{OA}}{C_{OA} + C_i^*(T)} \quad (8)$$

255 where C_{OA} is the concentration of OA measured by the SP-AMS, and $C_i^*(T)$ is the saturation
256 concentration of species i at temperature (T). The temperature-dependent $C_i^*(T)$ was obtained by
257 (Nie et al., 2022):

$$258 \quad \log_{10} C_i^*(T) = \log_{10} C_i^*(300K) + \frac{\Delta H_{vap,i}}{R \ln(10)} \left(\frac{1}{300} - \frac{1}{T} \right) \quad (9)$$

$$259 \quad \Delta H_{vap,i} = -5.7 \log_{10} C_i^*(300K) + 129 \quad (10)$$

260 where $\Delta H_{vap,i}$ is the enthalpy of vaporization and can be estimated based on $\log_{10} C_i^*(300K)$.

261 2.3.4 Estimation of the production rate of RO₂ and OH

262 A zero-dimensional box model (0-D Atmospheric Modeling, F0AM(Wolfe et al., 2016)) based
263 on Master Chemical Mechanism (MCM v3.1.1, <https://mcm.york.ac.uk/MCM>) was used to simulate
264 the production rate of OH in this study. The F0AM box model has been widely used in investigating

265 chemical reactions of VOCs, NO_x, and RO_x radicals (including OH, HO₂, and RO₂) in field and
266 laboratory researches (Baublitz et al., 2023; Yang et al., 2022; D'ambro et al., 2017). The simulation
267 was constrained with the observation data of non-methane hydrocarbons (NMHC), HCHO,
268 CH₃CHO, NO, CO, HONO, and meteorological parameters (RH, temperature, photolysis rates, and
269 pressure). The background concentration of CH₄ was set as 1.8 ppm (Wang et al., 2011). The
270 simulation time step was set to be 5 minutes. With respect to the integrity and temporal coverage of
271 the observation data, the simulation period was from 16 October to 16 November 2019. Further
272 details on model settings can be found in Yang et al. (2022)

273 The empirical kinetic modeling approach (EKMA) is applied to investigate the sensitivity of
274 the production rate of RO₂ and OH to the variation of NO_x and VOCs. The base case was simulated
275 based on the observation of average conditions. Sensitivity tests are performed by adjusting NO_x or
276 VOCs by a ratio ranging from 0.1 to 2.0 without changing other parameters.

277 **3. Results and discussion**

278 **3.1 Overview**

279 Figure 1 shows the temporal profile of particle number size distribution (PNSD) and
280 condensation sink (CS) during the measurement (a), one-dimensional thermograms and T_{max}
281 measured by the FIGAERO-CIMS (b), bulk PM₁ chemical composition measured by the SP-AMS
282 and PM₁ concentration (c), deconvolved OA factors from PMF analysis (d), and wind speed and
283 direction (e). Note that all measurements started on 2 October. As shown in Fig. 1a, new particle
284 formation (NPF) events occurred frequently along with relatively low CS values during the
285 measurement period (44.4%, 20 out of 45 days). The T_{max} mainly varied in two temperature ranges,
286 80-95 °C and 110-120°C (Fig. 1b). The lower T_{max} was usually accompanied by high desorption
287 signals peaked at 80-95 °C (Fig. 1b), a higher fraction of LOOA (Fig. 1d), and an obvious wide
288 accumulation mode in PNSD (Fig. 1a).

289 The evening peak of hydrocarbon-like OA (HOA) and biomass burning OA (BBOA) was
290 related to local anthropogenic activities (e.g., biomass burning, cooking, and traffic, Fig. 2). The
291 less oxygenated OA (LOOA) and biomass burning SOA (BBSOA) showed afternoon peaks (Fig.

292 2), which could be attributed to secondary organic aerosol (SOA) formation through daytime
293 photochemical reactions. LOOA showed a noticeable increase corresponding to the particle surface
294 area (Fig. S8), while we did not observe such correlation for other SOA factors (MOOA and
295 BBSOA). Furthermore, LOOA exhibited a stronger positive correlation with organic vapors
296 measured by the FIGAERO-CIMS compared to other OA factors (Fig. S9). These results suggested
297 that the daytime formation of LOOA was attributed to gas-particle partitioning. The O_x ($O_x=O_3+NO_2$)
298 had a strong correlation with organic vapors in the afternoon (10:00-16:00 LT, Fig. S10),
299 highlighting an important role of photochemical reaction on the formation of LOOA.

300 The high desorption signal at a lower temperature range suggested that the volatility of OA
301 could be higher, which could be associated with the formation of LOOA. Coincidentally, either NPF
302 events or a higher fraction of LOOA could only be observed during the period prevalent with north
303 wind direction (Fig. 1e), when the measurement site was affected by the pollutant from the city
304 cluster around Guangzhou city. It indicates that the urban pollutants might promote particle
305 formation and growth and daytime SOA formation by increasing oxidants and acting as precursor
306 gases. Xiao et al. (2023) suggested that fresh urban emissions could enhance NPF, while NPF was
307 suppressed in aged urban plumes. Shrivastava et al. (2019) found that urban emissions, including
308 NO_x and oxidants, could significantly enhance the SOA formation in the Amazon rainforest. Three
309 periods were classified based on the combination of wind direction and the analysis of backward
310 trajectories to further investigate the impact of urban pollutants on this downwind site, which were
311 long-range transport, urban air masses, and coastal air masses periods (Fig. S2 and Table. S2). The
312 long-range transport period was related to long-range transport masses from northeast inland. The
313 urban air masses period was mainly affected by regional urban air masses from the PRD region. The
314 coastal air masses period was associated with air masses from the South China Sea and the northeast
315 coast.

316 A significant daytime peak of LOOA ($10.4 \mu\text{g m}^{-3}$) was shown during the urban air masses
317 period (Fig. 2c), while the enhancement of BBSOA was inapparent. It suggests that the contribution
318 of gas-particle reactions on SOA formation was enhanced when the site was affected by urban
319 plumes. The O_x concentration in the afternoon during the urban air masses period was higher than
320 that during the long-range transport period (Fig. S11), which might be able to explain the significant
321 enhancement of LOOA for the urban air masses period. These results imply that urban pollution

322 plumes could promote the formation of SOA in the downwind region by increasing the oxidant
323 concentration.

324 **3.2 The daytime formation of FIGAERO OA**

325 As aforementioned, the increase of LOOA was usually along with the significant desorption
326 signals measured by the FIGAERO-CIMS at a low temperature range (80-95°C), suggesting that
327 OA volatility could be higher. The average two-dimensional thermograms of all calibrated and semi-
328 quantified species and an example of a one-dimensional thermogram of levoglucosan can be found
329 in Fig. 3 a and b, respectively. According to Eqs. (1) and (2), we calculated the C^* value of all
330 calibrated and semi-quantified species based on their T_{max} and constructed volatility distribution as
331 volatility basis set (VBS, Fig. 3c). The T_{max} of each species is obtained based on their average
332 thermogram. These 12 VBS bins were classified into three groups (Donahue et al., 2012): semi-
333 volatile organic compounds (SVOC, $0.3 < C^* \leq 3 \times 10^2 \mu\text{g m}^{-3}$), less-volatile organic compounds
334 (LVOC, $3 \times 10^{-4} < C^* \leq 0.3 \mu\text{g m}^{-3}$), and extremely low-volatility organic compounds (ELVOC,
335 $C^* \leq 3 \times 10^{-4} \mu\text{g m}^{-3}$). In general, most species measured by FIGAERO-CIMS fall into LVOC groups
336 (Fig. S12). Note that the decomposition of organic compounds was ignored in this method, which
337 could affect thermogram peaks in some cases and the measurement of low volatility compounds
338 (Wang and Hildebrandt Ruiz, 2018). Furthermore, the fraction of SVOC might be underestimated
339 owing to its high volatility, as a result fast evaporation could occur during the collection on the filter
340 and shifting from sampling mode to desorption mode.

341 During the urban air masses period, the FIGAERO-CIMS measured significant signals at a
342 desorption temperature range of SVOC and LVOC (Fig. S13) in the afternoon (12:00-16:00 LT),
343 indicating that the OA volatility could be higher. The SVOC+LVOC in the FIGAERO OA increased
344 from $5.2 \mu\text{g m}^{-3}$ (8:00 LT) to $16.29 \mu\text{g m}^{-3}$ (15:00 LT) during the urban air masses period (Fig. 4a),
345 which was coincident with an enhancement of LOOA (Fig. 2c). It suggested that daytime
346 enhancement of the SVOC+LVOC in the FIGAERO OA was closely related to the obvious LOOA
347 formation. The FIGAERO OA during the urban air masses period was systemically higher than that
348 during the long-range transport period, with a significantly higher concentration of LVOC group
349 (Fig. 4b), especially the portion with a volatility $\log_{10}C^*$ of -1. Table 1 investigated the relationship

350 between SVOC+LVOC and six OA factors. The SVOC+LVOC in FIGAERO OA had a significant
351 positive correlation ($R=0.72-0.85$) with the LOOA, especially during the urban air masses period
352 ($R=0.85$, Fig. S14 and Table 1), suggesting that the LOOA formation was mainly responsible for
353 the increase of OA volatility.

354 Interestingly, the high volatility organic vapors (SVOC+IVOC+VOC, $C^* > 0.3 \mu\text{g m}^{-3}$)
355 dramatically increased in the afternoon during the urban air masses period, while we did not observe
356 such phenomenon for low volatility (ELVOC+LVOC, $C^* \leq 0.3 \mu\text{g m}^{-3}$) organic vapors (Fig. 4c).
357 The concentration of low volatility organic vapors in the afternoon (12:00-16:00 LT) did not show
358 a significant difference (1.76 and $1.84 \mu\text{g m}^{-3}$) between the long-range transport and urban air masses
359 periods, indicating that the irreversible condensation of low volatility organic vapors could not fully
360 explain the enhancement of LOOA during the urban air masses period (Wang et al., 2022). However,
361 the high volatility organic vapors had a notably higher concentration ($51.69 \mu\text{g m}^{-3}$) during the urban
362 air masses period than that ($41.70 \mu\text{g m}^{-3}$) during the long-range transport period. It implies that the
363 significant enhancement of LOOA during the urban air masses period might be mainly attributed to
364 the equilibrium partitioning of high volatility organic vapors, which could also increase the volatility
365 of total OA.

366 Here we selected a typical day (2 November 2019) of the urban air masses period for further
367 investigation. The measurement site was affected by the urban plume from the city cluster in the
368 PRD region on this day (Fig. S15). A wide accumulation mode centered at about 180 nm in PNSD
369 was observed, with a significant desorption signal measured by the FIGAERO-CIMS in the
370 afternoon and weak north wind (Fig. S16). As shown in Fig. 5a, the desorption signals of organic
371 compounds increased from 9:00 LT and reached their peak at 14:00 LT, suggesting a significant
372 daytime SOA formation. The variation of OA volatility distribution and mean $C^*(\overline{C^*})$ is shown in
373 Fig. 5b. The $\overline{C^*}$ shown an afternoon peak ($0.021 \mu\text{g m}^{-3}$) at 15:00 LT, suggesting a higher OA
374 volatility in the afternoon. An evident enhancement of OA with a volatility $\log_{10}C^*$ of -1 was
375 observed in the afternoon, aligning with the formation of LOOA (Fig. 5c), which primarily
376 contributes to higher OA volatility. Combined with the volatility distribution analysis in Fig. 4b, it
377 indicated that the main components of LOOA have a volatility $\log_{10}C^*$ of -1. Interestingly, the
378 T_{max} value of the sum thermogram (Fig. 5a) increased from 81°C at 9:00 to 96°C at 17:00, implying
379 that the OA volatility decreased during the daytime owing to the daytime aging processes. However,

380 the $\overline{C^*}$ value consistently increased from 6:00 LT until 15:00 LT and then began to decrease, which
381 was in conflict with the increasing T_{max} . One possible reason is that species in the FIGAERO OA
382 fell into a specific T_{max} range (about 11°C) were categorized into different C^* bins by a factor of
383 10. Thus, the slight variation of T_{max} might not affect the estimated volatility distribution of
384 FIGAERO OA. The other possible reason is that the volatility distribution of FIGAERO OA was
385 estimated based on the T_{max} value of calibrated and semi-quantified species, while the sum
386 thermograms contained all organic compounds containing C, H, and O atmos. There could be some
387 organic compounds formed through aging processes that were not included in the C^* estimation.

388 3.3 The contribution of high volatility organic vapors to SOA formations

389 In the previous section, we found that the significant enhancements in LOOA during the urban
390 air masses period might be attributed to the high volatility organic vapors through gas-particle
391 partitioning. The contribution of high volatility organic vapors to the OA concentration via
392 equilibrium partitioning can be estimated based on eq. (7). Our results show that the estimated
393 contribution of high volatility organic vapors (estimated $OA_{HV, gas}$) was higher (peaked at about 1.17
394 $\mu\text{g m}^{-3}$) during the urban air masses period (Fig. 6a). Correspondingly, we observed an enhancement
395 in the measured concentration of these species in the particle-phase (measured $OA_{HV, gas}$, peaked at
396 about 10.32 $\mu\text{g m}^{-3}$, Fig. 6b). This implies that the increase in high volatility organic vapors might
397 significantly contribute to the daytime SOA formation during the urban air masses period. However,
398 the estimated contribution was much lower than the measured value. It suggests that using the
399 equilibrium equation might not be able to fully explain the increase of LOOA contributed by the
400 high volatility organic vapors during the urban air masses period. Nie et al. (2022) indicated that the
401 estimation of OA contribution through the equilibrium equation can be easily disturbed by varied
402 meteorological processes, which would lead to uncertainties in the calculations.

403 Moreover, the gas-particle equilibrium theory assumes that particles are droplets and that the
404 high volatility species in the particle-phase could reach a reversible equilibrium with the gas-phase
405 concentration. However, some studies indicate that this assumption significantly overestimates the
406 volatility of these species in the particle-phase and underestimate the contribution of high volatility
407 organic vapors to the SOA concentration (Kolesar et al., 2015; Cappa and Wilson, 2011). This is

408 because particles might exist in a glassy state rather than a liquid state. It was consistent with the
409 difference of the volatility distribution of these species between the particle- and gas-phase (Fig.
410 7a). The volatility in the particle-phase was centered at a $\log_{10}C^*$ of -1, while that in the gas-phase
411 showed a higher concentration of $\log_{10}C^*=6-8 \mu\text{g m}^{-3}$, implying that the volatility of these
412 compounds in the particle-phase could be lower than that in the gas-phase.

413 Another possible explanation is that the corresponding species in the particle-phase could be
414 the decomposition products of low volatility compounds, leading to a higher concentration than
415 expected. We further investigate the difference between the measured and estimated concentration
416 of different high volatility species (Fig. 7b). The measured concentration was systematically higher
417 than the estimated value. The higher measured concentration of $\text{C}_2\text{H}_2\text{O}_4\text{I}^-$ could be owing to the
418 decomposition of low volatility species, as the desorption signal peaked at the ELVOC region (Fig.
419 7c). However, for higher molecular weight compounds, the corresponding T_{max} values were in the
420 LVOC region, suggesting that these species might not be the decomposition products. This implies
421 that the decomposition products might play a minor effect in the difference between the measured
422 and estimated concentration.

423 Taken together, these results suggest the increase in high volatility organic vapors could
424 promote the daytime enhancement of SOA during urban air masses period. However, this
425 contribution might be underestimated using gas-particle equilibrium theory, since the volatility of
426 organic aerosol may differ significantly from the volatility determined by the equilibrium theory.

427 **3.4 Enhancement of SOA formation by urban pollutants**

428 As aforementioned, the significant enhancement of high volatility organic vapors were
429 observed during the urban air masses period. Figure 8 compares the difference of organic vapors in
430 the carbon oxidation state (\overline{OS}_C) in the afternoon (12:00-16:00 LT) between the long-range transport
431 and urban air masses periods. A higher concentration of organic vapors with a low \overline{OS}_C ($\overline{OS}_C \leq 0$)
432 was observed during the urban air masses period, while this trend became to overturn for high \overline{OS}_C
433 ($\overline{OS}_C > 0$) organic vapors. It suggests that the oxidation degree of organic vapors was lower during
434 the urban air masses period, even though the O_x concentration was higher (Fig. S11). This trend was
435 more significant for compounds with carbon numbers between 2 and 5, indicating a higher

436 concentration of small molecules with low \overline{OS}_C during urban air masses period. The \overline{OS}_C of major
437 C₅ compounds was about -1.33, which was mainly contributed by C₅H₈NOI⁺, highlighting the role
438 of NO_x chemistry. The oxygenated organic vapors production rates depend on oxidant and precursor
439 concentration, and the mechanism of significant enhancement of high volatility organic vapors
440 remain unclear. We speculated that it could be partly attributed to the elevated NO_x concentration in
441 the afternoon during the urban air masses period (Fig. S17). NO_x was found to have a detrimental
442 effect on the production of highly oxidized products, and thus the formation of low volatility vapors
443 (Rissanen, 2018), which might be responsible for the smooth increase of low volatility organic
444 vapors. Previous studies found that the increase of NO_x could lead to higher OH production, which
445 would offset decreases in the autoxidation efficiency and further result in enhanced SOA formation
446 (Liu et al., 2021; Pye et al., 2019). During the urban air masses period, both low volatility and high
447 volatility CHON compounds increased in the afternoon, implying the effect of NO_x on the
448 photochemical reactions (Fig. S18 a and b). That was further evidenced by the higher fraction of
449 CHON compounds in the FIGAERO OA (Fig. S18f). This result was consistent with Schwantes et
450 al. (2019), who reported that low volatility organic nitrates might have a significant contribution to
451 SOA under high NO_x conditions. Interestingly, in contrast with the higher fraction of low volatility
452 CHON compounds in the afternoon, the fraction of high volatility CHON compounds was lower at
453 the same time (Fig. S18 d and e), indicating that the effect of high NO_x concentration on
454 photochemical oxidation goes beyond the formation of CHON compounds for high volatility
455 species.

456 To further understand how the urban plumes affect the SOA formation, we used an observation-
457 constrained box model to simulate the production rate of organic peroxy radicals (RO₂) and OH
458 with different NO_x and VOCs concentrations (Fig. 9). The detailed description of the box model is
459 described in Sect. 2.3.4. In general, the production rates of OH (P(OH)) were close to the transition
460 regime during three selected periods (Fig. 9a), where the P(OH) is sensitive to both VOCs and NO_x
461 variation. Further, the P(OH) tended to be in the NO_x-limited regime during the coastal air masses
462 period. The emission of NO_x might enhance the atmospheric oxidation capacity, consistent with the
463 results from other observations (Shrivastava et al., 2019; Pye et al., 2019). Interestingly, the
464 sensitivity regime of P(OH) changed to the VOCs-limited during the urban air masses period,
465 suggesting that the production of OH would be suppressed with continued increases in NO_x. During

466 the urban air masses period, the concentration of NO_x and VOCs was noticeably increased compared
467 to the coastal air masses period, leading to a significant increase of $\text{P}(\text{OH})$.

468 Recent studies show that autooxidation of RO_2 can result in highly oxygenated molecules
469 ($\text{O}:\text{C} \geq 0.7$) and promote SOA formation (Pye et al., 2019; Pye et al., 2015). In general, the production
470 rate of RO_2 ($\text{P}(\text{RO}_2)$) was in the VOCs-limited regime during three selected periods (Fig. 9b), where
471 the $\text{P}(\text{RO}_2)$ increased with the increase of VOCs. It suggests that the production of RO_2 was
472 suppressed with the increase in NO_x . During the urban air masses period, the concentration of VOCs
473 was noticeably increased compared to the coastal air masses period, leading to a significant increase
474 of $\text{P}(\text{RO}_2)$. The model results indicate that urban pollutants, including NO_x and VOCs, could
475 enhance the oxidizing capacity, while the increase of VOCs was mainly responsible for significant
476 daytime SOA formation.

477 **4. Conclusions**

478 In this study, we demonstrated that daytime SOA formation could be enhanced when the rural
479 site was affected by pollutants from the city region, which could be partly attributed to the high
480 concentration of oxidant in the urban pollution. A higher volatility of OA was observed during the
481 urban air masses period, which was mainly contributed by the component with a volatility $\log_{10} C^*$
482 of -1. The significant increase of SVOC+LVOC in FIGAERO OA in the afternoon was associated
483 with enhanced LOOA formation. Similar to other measurements, the daytime formation of LOOA
484 was mainly through gas-to-particle partitioning of organic vapors, supported by a significant
485 positive relationship between the LOOA and organic vapors. We observed a dramatic increase in
486 the high volatility organic vapors in the afternoon during the urban air masses period, while low
487 volatility organic vapors did not exhibit a similar growth trend. It indicated that the rapid increase
488 of LOOA during the urban air masses period was mainly contributed by the gas-particle partitioning
489 of high volatility organic vapors. However, this contribution was underestimated using equilibrium
490 theory, since the volatility of high organic vapors in the particle phase was significantly lower than
491 that in the gas-phase.

492 The high NO_x might also suppress the formation of highly oxidized products. Thus, the
493 elevated NO_x in the urban plume might be able to explain the smooth increase in low volatility

494 organic vapors and a higher concentration of organic vapors with a low \overline{OS}_C . Box model simulation
495 showed that the P(OH) were close to the transition regime during three selected periods, indicating
496 that the elevated NO_x and VOCs in urban plumes can increase the oxidizing capacity. However, the
497 P(RO₂) was in the VOCs-limited regime, suggesting that the increase in VOCs was mainly
498 responsible for the daytime enhancement of SOA. Further investigations on the effect of urban
499 pollutants on SOA formation on the regional scale are still needed for formulating air pollution
500 control strategies.

501

502 *Data availability.* Data from the measurements are available at
503 <https://doi.org/10.6084/m9.figshare.25376059>.

504

505 *Supplement.* The supplement related to this article is available online at xxx.

506

507 *Author contributions.* **MC, YC, and BY** designed the research. **MC, YC, BY, SH, EZ, ZW, YL,**
508 **TL, WH, WC, QS, WL, YP, BL, QS, and JZ** performed the measurements. **MC, YC, BY, SH,**
509 **EZ, SY, ZW, YL, TL, WH, WC, QS, WL, YP, BL, QS, and JZ** analyzed the data. **MC, YC, and**
510 **BY** wrote the paper with contributions from all co-authors.

511

512 *Competing interests.* The authors declare that they have no conflict of interest.

513

514 *Acknowledgment.* Additional support from the crew of the Heshan supersite and Guangdong
515 Environmental Monitoring Center is greatly acknowledged.

516

517 *Financial support.* This work was supported by the National Key R&D Plan of China (grant no.
518 2019YFC0214605, 2019YFE0106300, and 2018YFC0213904), the Key-Area Research and
519 Development Program of Guangdong Province (grant no. 2019B110206001), the National Natural
520 Science Foundation of China (grant nos. 42305123, 41877302, 91644225, 41775117 and 41807302),
521 Guangdong Natural Science Funds for Distinguished Young Scholar (grant no. 2018B030306037),
522 Guangdong Innovative and Entrepreneurial Research Team Program (grant no. 2016ZT06N263),
523 Guangdong Province Key Laboratory for Climate Change and Natural Disaster Studies (grant no.

524 2020B1212060025), Guangdong Basic and Applied Basic Research Foundation (grant nos.
525 2019A151511079, 2019A1515110791, 2023A1515012240, and 2024A1515030221), Science and
526 Technology Research project of Guangdong Meteorological Bureau (grant no. GRMC2018M07),
527 the Natural Science Foundation of Guangdong Province, China (grant no. 2016A030311007), the
528 Research Fund Program of Guangdong-Hongkong-Macau Joint Laboratory of Collaborative
529 Innovation for Environmental Quality (grant no. GHML2022-005), Science and Technology
530 Innovation Team Plan of Guangdong Meteorological Bureau (grant no. GRMCTD202003), and
531 Science and Technology Program of Guangdong Province (Science and Technology Innovation
532 Platform Category, No. 2019B121201002).
533

534 **References**

535 Apte, J. S., Brauer, M., Cohen, A. J., Ezzati, M., and Pope, C. A., III: Ambient PM_{2.5} Reduces
536 Global and Regional Life Expectancy, *Environmental Science & Technology Letters*, 5, 546-551,
537 10.1021/acs.estlett.8b00360, 2018.

538 Arias, P., Bellouin, N., Coppola, E., Jones, R., Krinner, G., Marotzke, J., Naik, V., Palmer, M.,
539 Plattner, G.-K., Rogelj, J., Rojas, M., Sillmann, J., Storelvmo, T., Thorne, P., Trewin, B., Rao, K.,
540 Adhikary, B., Allan, R., Armour, K., and Zickfeld, K.: IPCC AR6 WGI Technical Summary, in, In
541 Press.

542 Baublitz, C. B., Fiore, A. M., Ludwig, S. M., Nicely, J. M., Wolfe, G. M., Murray, L. T.,
543 Commane, R., Prather, M. J., Anderson, D. C., Correa, G., Duncan, B. N., Follette-Cook, M.,
544 Westervelt, D. M., Bourgeois, I., Brune, W. H., Bui, T. P., DiGangi, J. P., Diskin, G. S., Hall, S. R.,
545 McKain, K., Miller, D. O., Peischl, J., Thames, A. B., Thompson, C. R., Ullmann, K., and Wofsy,
546 S. C.: An observation-based, reduced-form model for oxidation in the remote marine troposphere,
547 *Proceedings of the National Academy of Sciences*, 120, e2209735120, 10.1073/pnas.2209735120,
548 2023.

549 Bertrand, A., Stefenelli, G., Jen, C. N., Pieber, S. M., Bruns, E. A., Ni, H., Temime-Roussel,
550 B., Slowik, J. G., Goldstein, A. H., El Haddad, I., Baltensperger, U., Prévôt, A. S. H., Wortham, H.,
551 and Marchand, N.: Evolution of the chemical fingerprint of biomass burning organic aerosol during
552 aging, *Atmos. Chem. Phys.*, 18, 7607-7624, 10.5194/acp-18-7607-2018, 2018.

553 Bianchi, F., Kurtén, T., Riva, M., Mohr, C., Rissanen, M. P., Roldin, P., Berndt, T., Crouse, J.
554 D., Wennberg, P. O., Mentel, T. F., Wildt, J., Junninen, H., Jokinen, T., Kulmala, M., Worsnop, D.
555 R., Thornton, J. A., Donahue, N., Kjaergaard, H. G., and Ehn, M.: Highly Oxygenated Organic
556 Molecules (HOM) from Gas-Phase Autoxidation Involving Peroxy Radicals: A Key Contributor to
557 Atmospheric Aerosol, *Chemical Reviews*, 119, 3472-3509, 10.1021/acs.chemrev.8b00395, 2019.

558 Buchholz, A., Ylisirniö, A., Huang, W., Mohr, C., Canagaratna, M., Worsnop, D. R.,
559 Schobesberger, S., and Virtanen, A.: Deconvolution of FIGAERO-CIMS thermal desorption
560 profiles using positive matrix factorisation to identify chemical and physical processes during
561 particle evaporation, *Atmos. Chem. Phys.*, 20, 7693-7716, 10.5194/acp-20-7693-2020, 2020.

562 Cai, M., Liang, B., Sun, Q., Liu, L., Yuan, B., Shao, M., Huang, S., Peng, Y., Wang, Z., Tan,
563 H., Li, F., Xu, H., Chen, D., and Zhao, J.: The important roles of surface tension and growth rate in
564 the contribution of new particle formation (NPF) to cloud condensation nuclei (CCN) number
565 concentration: evidence from field measurements in southern China, *Atmos. Chem. Phys.*, 21, 8575-
566 8592, 10.5194/acp-21-8575-2021, 2021.

567 Cai, M., Huang, S., Liang, B., Sun, Q., Liu, L., Yuan, B., Shao, M., Hu, W., Chen, W., Song,
568 Q., Li, W., Peng, Y., Wang, Z., Chen, D., Tan, H., Xu, H., Li, F., Deng, X., Deng, T., Sun, J., and
569 Zhao, J.: Measurement report: Distinct size dependence and diurnal variation in organic aerosol
570 hygroscopicity, volatility, and cloud condensation nuclei activity at a rural site in the Pearl River
571 Delta (PRD) region, China, *Atmos. Chem. Phys.*, 22, 8117-8136, 10.5194/acp-22-8117-2022, 2022.

572 Cai, Y., Ye, C., Chen, W., Hu, W., Song, W., Peng, Y., Huang, S., Qi, J., Wang, S., Wang, C.,
573 Wu, C., Wang, Z., Wang, B., Huang, X., He, L., Gligorovski, S., Yuan, B., Shao, M., and Wang, X.:
574 The important contribution of secondary formation and biomass burning to oxidized organic
575 nitrogen (OON) in a polluted urban area: insights from in situ measurements of a chemical

576 ionization mass spectrometer (CIMS), *Atmos. Chem. Phys.*, 23, 8855-8877, 10.5194/acp-23-8855-
577 2023, 2023.

578 Cappa, C. D. and Wilson, K. R.: Evolution of organic aerosol mass spectra upon heating:
579 implications for OA phase and partitioning behavior, *Atmos. Chem. Phys.*, 11, 1895-1911,
580 10.5194/acp-11-1895-2011, 2011.

581 Chen, Y., Takeuchi, M., Nah, T., Xu, L., Canagaratna, M. R., Stark, H., Baumann, K., Canonaco,
582 F., Prévôt, A. S. H., Huey, L. G., Weber, R. J., and Ng, N. L.: Chemical characterization of secondary
583 organic aerosol at a rural site in the southeastern US: insights from simultaneous high-resolution
584 time-of-flight aerosol mass spectrometer (HR-ToF-AMS) and FIGAERO chemical ionization mass
585 spectrometer (CIMS) measurements, *Atmos. Chem. Phys.*, 20, 8421-8440, 10.5194/acp-20-8421-
586 2020, 2020.

587 D'Ambro, E. L., Møller, K. H., Lopez-Hilfiker, F. D., Schobesberger, S., Liu, J., Shilling, J. E.,
588 Lee, B. H., Kjaergaard, H. G., and Thornton, J. A.: Isomerization of Second-Generation Isoprene
589 Peroxy Radicals: Epoxide Formation and Implications for Secondary Organic Aerosol Yields,
590 *Environmental Science & Technology*, 51, 4978-4987, 10.1021/acs.est.7b00460, 2017.

591 de Sá, S. S., Palm, B. B., Campuzano-Jost, P., Day, D. A., Hu, W., Isaacman-VanWertz, G., Yee,
592 L. D., Brito, J., Carbone, S., Ribeiro, I. O., Cirino, G. G., Liu, Y., Thalman, R., Sedlacek, A., Funk,
593 A., Schumacher, C., Shilling, J. E., Schneider, J., Artaxo, P., Goldstein, A. H., Souza, R. A. F., Wang,
594 J., McKinney, K. A., Barbosa, H., Alexander, M. L., Jimenez, J. L., and Martin, S. T.: Urban
595 influence on the concentration and composition of submicron particulate matter in central Amazonia,
596 *Atmos. Chem. Phys.*, 18, 12185-12206, 10.5194/acp-18-12185-2018, 2018.

597 Donahue, N. M., Epstein, S. A., Pandis, S. N., and Robinson, A. L.: A two-dimensional
598 volatility basis set: 1. organic-aerosol mixing thermodynamics, *Atmos. Chem. Phys.*, 11, 3303-3318,
599 10.5194/acp-11-3303-2011, 2011.

600 Donahue, N. M., Kroll, J. H., Pandis, S. N., and Robinson, A. L.: A two-dimensional volatility
601 basis set – Part 2: Diagnostics of organic-aerosol evolution, *Atmos. Chem. Phys.*, 12, 615-634,
602 10.5194/acp-12-615-2012, 2012.

603 Dong, H. B., Zeng, L. M., Hu, M., Wu, Y. S., Zhang, Y. H., Slanina, J., Zheng, M., Wang, Z.
604 F., and Jansen, R.: Technical Note: The application of an improved gas and aerosol collector for
605 ambient air pollutants in China, *Atmos. Chem. Phys.*, 12, 10519-10533, 10.5194/acp-12-10519-
606 2012, 2012.

607 Ervens, B., Turpin, B. J., and Weber, R. J.: Secondary organic aerosol formation in cloud
608 droplets and aqueous particles (aqSOA): a review of laboratory, field and model studies, *Atmos.*
609 *Chem. Phys.*, 11, 11069-11102, 10.5194/acp-11-11069-2011, 2011.

610 Fry, J. L., Brown, S. S., Middlebrook, A. M., Edwards, P. M., Campuzano-Jost, P., Day, D. A.,
611 Jimenez, J. L., Allen, H. M., Ryerson, T. B., Pollack, I., Graus, M., Warneke, C., de Gouw, J. A.,
612 Brock, C. A., Gilman, J., Lerner, B. M., Dubé, W. P., Liao, J., and Welti, A.: Secondary organic
613 aerosol (SOA) yields from NO₃ radical + isoprene based on nighttime aircraft power plant plume
614 transects, *Atmos. Chem. Phys.*, 18, 11663-11682, 10.5194/acp-18-11663-2018, 2018.

615 Hallquist, M., Wenger, J. C., Baltensperger, U., Rudich, Y., Simpson, D., Claeys, M., Dommen,
616 J., Donahue, N. M., George, C., Goldstein, A. H., Hamilton, J. F., Herrmann, H., Hoffmann, T.,
617 Iinuma, Y., Jang, M., Jenkin, M. E., Jimenez, J. L., Kiendler-Scharr, A., Maenhaut, W., McFiggans,
618 G., Mentel, T. F., Monod, A., Prévôt, A. S. H., Seinfeld, J. H., Surratt, J. D., Szmigielski, R., and
619 Wildt, J.: The formation, properties and impact of secondary organic aerosol: current and emerging

620 issues, *Atmos. Chem. Phys.*, 9, 5155-5236, 10.5194/acp-9-5155-2009, 2009.

621 Hodzic, A., Jimenez, J. L., Madronich, S., Canagaratna, M. R., DeCarlo, P. F., Kleinman, L.,
622 and Fast, J.: Modeling organic aerosols in a megacity: potential contribution of semi-volatile and
623 intermediate volatility primary organic compounds to secondary organic aerosol formation, *Atmos.*
624 *Chem. Phys.*, 10, 5491-5514, 10.5194/acp-10-5491-2010, 2010.

625 Huang, R.-J., Zhang, Y., Bozzetti, C., Ho, K.-F., Cao, J.-J., Han, Y., Daellenbach, K. R., Slowik,
626 J. G., Platt, S. M., Canonaco, F., Zotter, P., Wolf, R., Pieber, S. M., Bruns, E. A., Crippa, M., Ciarelli,
627 G., Piazzalunga, A., Schwikowski, M., Abbaszade, G., Schnelle-Kreis, J., Zimmermann, R., An, Z.,
628 Szidat, S., Baltensperger, U., Haddad, I. E., and Prevot, A. S. H.: High secondary aerosol
629 contribution to particulate pollution during haze events in China, *Nature*, 514, 218–222,
630 10.1038/nature13774
631 [http://www.nature.com/nature/journal/vaop/ncurrent/abs/nature13774.html#supplementary-](http://www.nature.com/nature/journal/vaop/ncurrent/abs/nature13774.html#supplementary-information)
632 [information](http://www.nature.com/nature/journal/vaop/ncurrent/abs/nature13774.html#supplementary-information), 2014.

633 Huang, W., Saathoff, H., Pajunoja, A., Shen, X., Naumann, K. H., Wagner, R., Virtanen, A.,
634 Leisner, T., and Mohr, C.: α -Pinene secondary organic aerosol at low temperature: chemical
635 composition and implications for particle viscosity, *Atmos. Chem. Phys.*, 18, 2883-2898,
636 10.5194/acp-18-2883-2018, 2018.

637 Iyer, S., Lopez-Hilfiker, F., Lee, B. H., Thornton, J. A., and Kurtén, T.: Modeling the Detection
638 of Organic and Inorganic Compounds Using Iodide-Based Chemical Ionization, *The Journal of*
639 *Physical Chemistry A*, 120, 576-587, 10.1021/acs.jpca.5b09837, 2016.

640 Kolesar, K. R., Li, Z., Wilson, K. R., and Cappa, C. D.: Heating-Induced Evaporation of Nine
641 Different Secondary Organic Aerosol Types, *Environmental Science & Technology*, 49, 12242-
642 12252, 10.1021/acs.est.5b03038, 2015.

643 Kuang, Y., Huang, S., Xue, B., Luo, B., Song, Q., Chen, W., Hu, W., Li, W., Zhao, P., Cai, M.,
644 Peng, Y., Qi, J., Li, T., Wang, S., Chen, D., Yue, D., Yuan, B., and Shao, M.: Contrasting effects of
645 secondary organic aerosol formations on organic aerosol hygroscopicity, *Atmos. Chem. Phys.*, 21,
646 10375-10391, 10.5194/acp-21-10375-2021, 2021.

647 Lanzafame, G. M., Srivastava, D., Favez, O., Bandowe, B. A. M., Shahpoury, P., Lammel, G.,
648 Bonnaire, N., Alleman, L. Y., Couvidat, F., Bessagnet, B., and Albinet, A.: One-year measurements
649 of secondary organic aerosol (SOA) markers in the Paris region (France): Concentrations,
650 gas/particle partitioning and SOA source apportionment, *Science of The Total Environment*, 757,
651 143921, <https://doi.org/10.1016/j.scitotenv.2020.143921>, 2021.

652 Le Breton, M., Wang, Y., Hallquist, Å. M., Pathak, R. K., Zheng, J., Yang, Y., Shang, D.,
653 Glasius, M., Bannan, T. J., Liu, Q., Chan, C. K., Percival, C. J., Zhu, W., Lou, S., Topping, D., Wang,
654 Y., Yu, J., Lu, K., Guo, S., Hu, M., and Hallquist, M.: Online gas- and particle-phase measurements
655 of organosulfates, organosulfonates and nitrooxy organosulfates in Beijing utilizing a FIGAERO
656 ToF-CIMS, *Atmos. Chem. Phys.*, 18, 10355-10371, 10.5194/acp-18-10355-2018, 2018.

657 Lee, B.-H., Kostenidou, E., Hildebrandt, L., Riipinen, I., Engelhart, G., Mohr, C., DeCarlo, P.,
658 Mihalopoulos, N., Prevot, A., Baltensperger, U. J. A. C., and Physics: Measurement of the ambient
659 organic aerosol volatility distribution: application during the Finokalia Aerosol Measurement
660 Experiment (FAME-2008), 10, 12149-12160, 2010.

661 Liu, Y., Seco, R., Kim, S., Guenther, A. B., Goldstein, A. H., Keutsch, F. N., Springston, S. R.,
662 Watson, T. B., Artaxo, P., Souza, R. A. F., McKinney, K. A., and Martin, S. T.: Isoprene photo-
663 oxidation products quantify the effect of pollution on hydroxyl radicals over Amazonia, *Science*

664 Advances, 4, eaar2547, doi:10.1126/sciadv.aar2547, 2018.

665 Liu, Y., Nie, W., Li, Y., Ge, D., Liu, C., Xu, Z., Chen, L., Wang, T., Wang, L., Sun, P., Qi, X.,
666 Wang, J., Xu, Z., Yuan, J., Yan, C., Zhang, Y., Huang, D., Wang, Z., Donahue, N. M., Worsnop, D.,
667 Chi, X., Ehn, M., and Ding, A.: Formation of condensable organic vapors from anthropogenic and
668 biogenic volatile organic compounds (VOCs) is strongly perturbed by NO_x in eastern China, *Atmos.*
669 *Chem. Phys.*, 21, 14789-14814, 10.5194/acp-21-14789-2021, 2021.

670 Lopez-Hilfiker, F. D., Iyer, S., Mohr, C., Lee, B. H., D'Ambro, E. L., Kurtén, T., and Thornton,
671 J. A.: Constraining the sensitivity of iodide adduct chemical ionization mass spectrometry to
672 multifunctional organic molecules using the collision limit and thermodynamic stability of iodide
673 ion adducts, *Atmos. Meas. Tech.*, 9, 1505-1512, 10.5194/amt-9-1505-2016, 2016.

674 Lopez-Hilfiker, F. D., Mohr, C., Ehn, M., Rubach, F., Kleist, E., Wildt, J., Mentel, T. F., Lutz,
675 A., Hallquist, M., Worsnop, D., and Thornton, J. A.: A novel method for online analysis of gas and
676 particle composition: description and evaluation of a Filter Inlet for Gases and AEROSols
677 (FIGAERO), *Atmos. Meas. Tech.*, 7, 983-1001, 10.5194/amt-7-983-2014, 2014.

678 Luo, B., Kuang, Y., Huang, S., Song, Q., Hu, W., Li, W., Peng, Y., Chen, D., Yue, D., Yuan, B.,
679 and Shao, M.: Parameterizations of size distribution and refractive index of biomass burning organic
680 aerosol with black carbon content, *Atmos. Chem. Phys.*, 22, 12401-12415, 10.5194/acp-22-12401-
681 2022, 2022.

682 Masoud, C. G., Li, Y., Wang, D. S., Katz, E. F., DeCarlo, P. F., Farmer, D. K., Vance, M. E.,
683 Shiraiwa, M., and Hildebrandt Ruiz, L.: Molecular composition and gas-particle partitioning of
684 indoor cooking aerosol: Insights from a FIGAERO-CIMS and kinetic aerosol modeling, *Aerosol*
685 *Science and Technology*, 56, 1156-1173, 10.1080/02786826.2022.2133593, 2022.

686 Mohr, C., Thornton, J. A., Heitto, A., Lopez-Hilfiker, F. D., Lutz, A., Riipinen, I., Hong, J.,
687 Donahue, N. M., Hallquist, M., and Petäjä, T. J. N. c.: Molecular identification of organic vapors
688 driving atmospheric nanoparticle growth, 10, 1-7, 2019.

689 Mutzel, A., Poulain, L., Berndt, T., Iinuma, Y., Rodigast, M., Böge, O., Richters, S., Spindler,
690 G., Sipilä, M., Jokinen, T., Kulmala, M., and Herrmann, H.: Highly Oxidized Multifunctional
691 Organic Compounds Observed in Tropospheric Particles: A Field and Laboratory Study,
692 *Environmental Science & Technology*, 49, 7754-7761, 10.1021/acs.est.5b00885, 2015.

693 Ng, N. L., Canagaratna, M. R., Jimenez, J. L., Zhang, Q., Ulbrich, I. M., and Worsnop, D. R.:
694 Real-Time Methods for Estimating Organic Component Mass Concentrations from Aerosol Mass
695 Spectrometer Data, *Environmental Science & Technology*, 45, 910-916, 10.1021/es102951k, 2011.

696 Nie, W., Yan, C., Huang, D. D., Wang, Z., Liu, Y., Qiao, X., Guo, Y., Tian, L., Zheng, P., Xu,
697 Z., Li, Y., Xu, Z., Qi, X., Sun, P., Wang, J., Zheng, F., Li, X., Yin, R., Dallenbach, K. R., Bianchi,
698 F., Petäjä, T., Zhang, Y., Wang, M., Schervish, M., Wang, S., Qiao, L., Wang, Q., Zhou, M., Wang,
699 H., Yu, C., Yao, D., Guo, H., Ye, P., Lee, S., Li, Y. J., Liu, Y., Chi, X., Kerminen, V.-M., Ehn, M.,
700 Donahue, N. M., Wang, T., Huang, C., Kulmala, M., Worsnop, D., Jiang, J., and Ding, A.: Secondary
701 organic aerosol formed by condensing anthropogenic vapours over China's megacities, *Nature*
702 *Geoscience*, 10.1038/s41561-022-00922-5, 2022.

703 Peng, Z., Lee-Taylor, J., Orlando, J. J., Tyndall, G. S., and Jimenez, J. L.: Organic peroxy
704 radical chemistry in oxidation flow reactors and environmental chambers and their atmospheric
705 relevance, *Atmos. Chem. Phys.*, 19, 813-834, 10.5194/acp-19-813-2019, 2019.

706 Philippin, S., Wiedensohler, A., and Stratmann, F.: Measurements of non-volatile fractions of
707 pollution aerosols with an eight-tube volatility tandem differential mobility analyzer (VTDMA-8),

708 Journal of Aerosol Science, 35, 185-203, <http://dx.doi.org/10.1016/j.jaerosci.2003.07.004>, 2004.

709 Praske, E., Otkjær, R. V., Crounse, J. D., Hethcox, J. C., Stoltz, B. M., Kjaergaard, H. G., and
710 Wennberg, P. O.: Atmospheric autoxidation is increasingly important in urban and suburban North
711 America, *Proceedings of the National Academy of Sciences*, 115, 64-69, 10.1073/pnas.1715540115,
712 2018.

713 Pye, H. O. T., Luecken, D. J., Xu, L., Boyd, C. M., Ng, N. L., Baker, K. R., Ayres, B. R., Bash,
714 J. O., Baumann, K., Carter, W. P. L., Edgerton, E., Fry, J. L., Hutzell, W. T., Schwede, D. B., and
715 Shepson, P. B.: Modeling the Current and Future Roles of Particulate Organic Nitrates in the
716 Southeastern United States, *Environmental Science & Technology*, 49, 14195-14203,
717 10.1021/acs.est.5b03738, 2015.

718 Pye, H. O. T., D'Ambro, E. L., Lee, B. H., Schobesberger, S., Takeuchi, M., Zhao, Y., Lopez-
719 Hilfiker, F., Liu, J., Shilling, J. E., Xing, J., Mathur, R., Middlebrook, A. M., Liao, J., Welti, A.,
720 Graus, M., Warneke, C., de Gouw, J. A., Holloway, J. S., Ryerson, T. B., Pollack, I. B., and Thornton,
721 J. A.: Anthropogenic enhancements to production of highly oxygenated molecules from
722 autoxidation, *Proceedings of the National Academy of Sciences*, 116, 6641-6646,
723 10.1073/pnas.1810774116, 2019.

724 Ren, S., Yao, L., Wang, Y., Yang, G., Liu, Y., Li, Y., Lu, Y., Wang, L., and Wang, L.: Volatility
725 parameterization of ambient organic aerosols at a rural site of the North China Plain, *Atmos. Chem.*
726 *Phys.*, 22, 9283-9297, 10.5194/acp-22-9283-2022, 2022.

727 Rissanen, M. P.: NO₂ Suppression of Autoxidation–Inhibition of Gas-Phase Highly Oxidized
728 Dimer Product Formation, *ACS Earth and Space Chemistry*, 2, 1211-1219,
729 10.1021/acsearthspacechem.8b00123, 2018.

730 Saha, P. K., Khlystov, A., Yahya, K., Zhang, Y., Xu, L., Ng, N. L., Grieshop, A. P. J. A. C., and
731 Physics: Quantifying the volatility of organic aerosol in the southeastern US, 17, 501-520, 2017.

732 Salvador, C. M. G., Tang, R., Priestley, M., Li, L., Tsiligiannis, E., Le Breton, M., Zhu, W.,
733 Zeng, L., Wang, H., Yu, Y., Hu, M., Guo, S., and Hallquist, M.: Ambient nitro-aromatic compounds
734 – biomass burning versus secondary formation in rural China, *Atmos. Chem. Phys.*, 21, 1389-1406,
735 10.5194/acp-21-1389-2021, 2021.

736 Schwantes, R. H., Charan, S. M., Bates, K. H., Huang, Y., Nguyen, T. B., Mai, H., Kong, W.,
737 Flagan, R. C., and Seinfeld, J. H.: Low-volatility compounds contribute significantly to isoprene
738 secondary organic aerosol (SOA) under high-NO_x conditions, *Atmos. Chem. Phys.*, 19, 7255-7278,
739 10.5194/acp-19-7255-2019, 2019.

740 Shrivastava, M., Andreae, M. O., Artaxo, P., Barbosa, H. M. J., Berg, L. K., Brito, J., Ching, J.,
741 Easter, R. C., Fan, J., Fast, J. D., Feng, Z., Fuentes, J. D., Glasius, M., Goldstein, A. H., Alves, E.
742 G., Gomes, H., Gu, D., Guenther, A., Jathar, S. H., Kim, S., Liu, Y., Lou, S., Martin, S. T., McNeill,
743 V. F., Medeiros, A., de Sá, S. S., Shilling, J. E., Springston, S. R., Souza, R. A. F., Thornton, J. A.,
744 Isaacman-VanWertz, G., Yee, L. D., Ynoue, R., Zaveri, R. A., Zelenyuk, A., and Zhao, C.: Urban
745 pollution greatly enhances formation of natural aerosols over the Amazon rainforest, *Nature*
746 *Communications*, 10, 1046, 10.1038/s41467-019-08909-4, 2019.

747 Wang, D. S. and Hildebrandt Ruiz, L.: Chlorine-initiated oxidation of n-alkanes under high-
748 NO_x conditions: insights into secondary organic aerosol composition and volatility using a
749 FIGAERO–CIMS, *Atmos. Chem. Phys.*, 18, 15535-15553, 10.5194/acp-18-15535-2018, 2018.

750 Wang, Y., Zhang, Y., Hao, J., and Luo, M.: Seasonal and spatial variability of surface ozone
751 over China: contributions from background and domestic pollution, *Atmos. Chem. Phys.*, 11, 3511-

752 3525, 10.5194/acp-11-3511-2011, 2011.

753 Wang, Y., Hu, M., Wang, Y., Zheng, J., Shang, D., Yang, Y., Liu, Y., Li, X., Tang, R., Zhu, W.,
754 Du, Z., Wu, Y., Guo, S., Wu, Z., Lou, S., Hallquist, M., and Yu, J. Z.: The formation of nitro-aromatic
755 compounds under high NO_x and anthropogenic VOC conditions in urban Beijing, China, *Atmos.*
756 *Chem. Phys.*, 19, 7649-7665, 10.5194/acp-19-7649-2019, 2019.

757 Wang, Y., Clusius, P., Yan, C., Dällenbach, K., Yin, R., Wang, M., He, X.-C., Chu, B., Lu, Y.,
758 Dada, L., Kangasluoma, J., Rantala, P., Deng, C., Lin, Z., Wang, W., Yao, L., Fan, X., Du, W., Cai,
759 J., Heikkinen, L., Tham, Y. J., Zha, Q., Ling, Z., Junninen, H., Petäjä, T., Ge, M., Wang, Y., He, H.,
760 Worsnop, D. R., Kerminen, V.-M., Bianchi, F., Wang, L., Jiang, J., Liu, Y., Boy, M., Ehn, M.,
761 Donahue, N. M., and Kulmala, M.: Molecular Composition of Oxygenated Organic Molecules and
762 Their Contributions to Organic Aerosol in Beijing, *Environmental Science & Technology*, 56, 770-
763 778, 10.1021/acs.est.1c05191, 2022.

764 Wolfe, G. M., Marvin, M. R., Roberts, S. J., Travis, K. R., and Liao, J.: The Framework for 0-
765 D Atmospheric Modeling (F0AM) v3.1, *Geosci. Model Dev.*, 9, 3309-3319, 10.5194/gmd-9-3309-
766 2016, 2016.

767 Xiao, Q., Zhang, J., Wang, Y., Ziemba, L. D., Crosbie, E., Winstead, E. L., Robinson, C. E.,
768 DiGangi, J. P., Diskin, G. S., Reid, J. S., Schmidt, K. S., Sorooshian, A., Hilario, M. R. A., Woods,
769 S., Lawson, P., Stamnes, S. A., and Wang, J.: New particle formation in the tropical free troposphere
770 during CAMP2Ex: statistics and impact of emission sources, convective activity, and synoptic
771 conditions, *Atmos. Chem. Phys.*, 23, 9853-9871, 10.5194/acp-23-9853-2023, 2023.

772 Yang, S., Yuan, B., Peng, Y., Huang, S., Chen, W., Hu, W., Pei, C., Zhou, J., Parrish, D. D.,
773 Wang, W., He, X., Cheng, C., Li, X. B., Yang, X., Song, Y., Wang, H., Qi, J., Wang, B., Wang, C.,
774 Wang, C., Wang, Z., Li, T., Zheng, E., Wang, S., Wu, C., Cai, M., Ye, C., Song, W., Cheng, P., Chen,
775 D., Wang, X., Zhang, Z., Wang, X., Zheng, J., and Shao, M.: The formation and mitigation of nitrate
776 pollution: comparison between urban and suburban environments, *Atmos. Chem. Phys.*, 22, 4539-
777 4556, 10.5194/acp-22-4539-2022, 2022.

778 Ye, C., Yuan, B., Lin, Y., Wang, Z., Hu, W., Li, T., Chen, W., Wu, C., Wang, C., Huang, S., Qi,
779 J., Wang, B., Wang, C., Song, W., Wang, X., Zheng, E., Krechmer, J. E., Ye, P., Zhang, Z., Wang,
780 X., Worsnop, D. R., and Shao, M.: Chemical characterization of oxygenated organic compounds in
781 the gas phase and particle phase using iodide CIMS with FIGAERO in urban air, *Atmos. Chem.*
782 *Phys.*, 21, 8455-8478, 10.5194/acp-21-8455-2021, 2021.

783 Ylisirniö, A., Buchholz, A., Mohr, C., Li, Z., Barreira, L., Lambe, A., Faiola, C., Kari, E., Yli-
784 Juuti, T., Nizkorodov, S. A., Worsnop, D. R., Virtanen, A., and Schobesberger, S.: Composition and
785 volatility of secondary organic aerosol (SOA) formed from oxidation of real tree emissions
786 compared to simplified volatile organic compound (VOC) systems, *Atmos. Chem. Phys.*, 20, 5629-
787 5644, 10.5194/acp-20-5629-2020, 2020.

788 Zhang, Q., Zheng, Y., Tong, D., Shao, M., Wang, S., Zhang, Y., Xu, X., Wang, J., He, H., Liu,
789 W., Ding, Y., Lei, Y., Li, J., Wang, Z., Zhang, X., Wang, Y., Cheng, J., Liu, Y., Shi, Q., Yan, L., Geng,
790 G., Hong, C., Li, M., Liu, F., Zheng, B., Cao, J., Ding, A., Gao, J., Fu, Q., Huo, J., Liu, B., Liu, Z.,
791 Yang, F., He, K., and Hao, J.: Drivers of improved PM_{2.5} air quality in China from 2013 to 2017,
792 *Proceedings of the National Academy of Sciences*, 116, 24463-24469, 10.1073/pnas.1907956116,
793 2019.

794

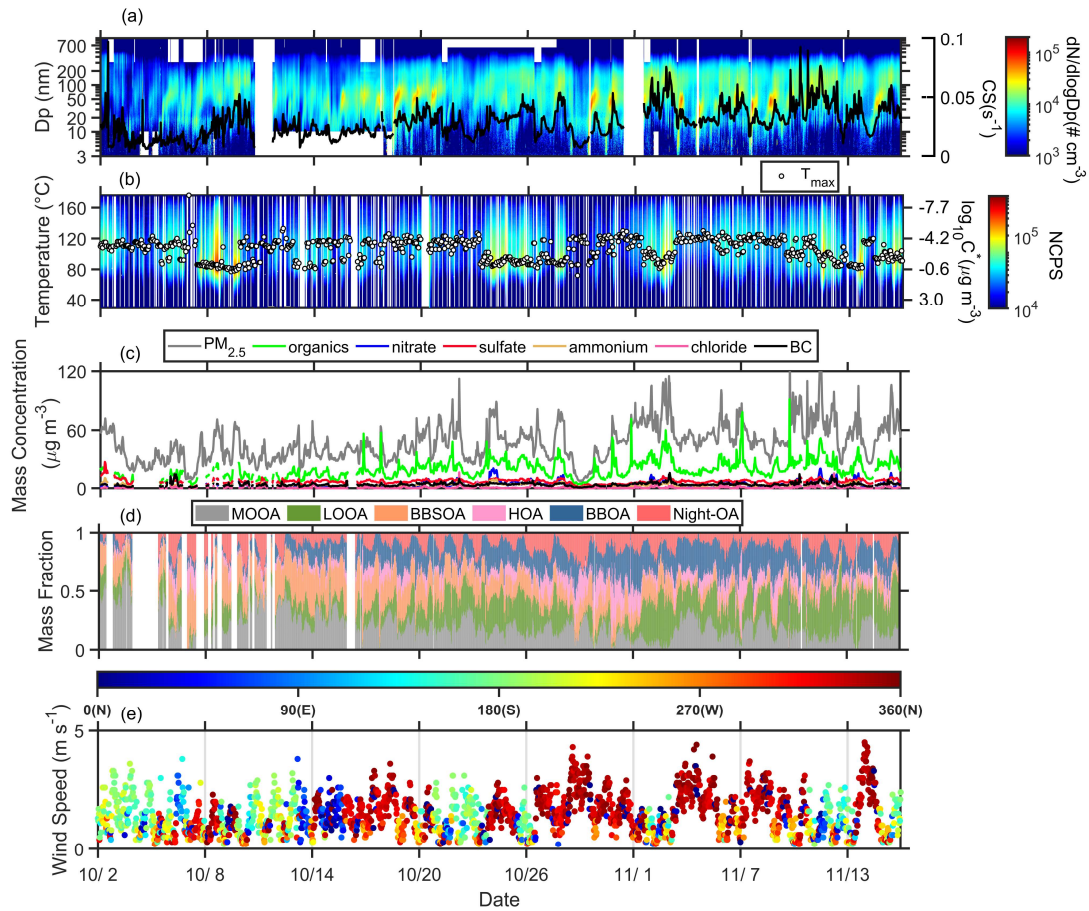
795

796 **Table 1.** The correlation coefficient between SVOC+LVOC in FIGAERO OA and six OA factors
797 in AMS OA during different periods.

	All campaign	Long-range Transport	Urban Air Masses	Coastal Air Masses
MOOA	-0.004	0.02	0.11	-0.19
LOOA	0.83	0.74	0.85	0.72
BBSOA	0.47	0.48	0.75	0.14
HOA	0.11	0.18	-0.11	0.61
BBOA	0.57	0.55	0.55	0.77
Night-OA	0.35	0.39	0.07	0.53

798

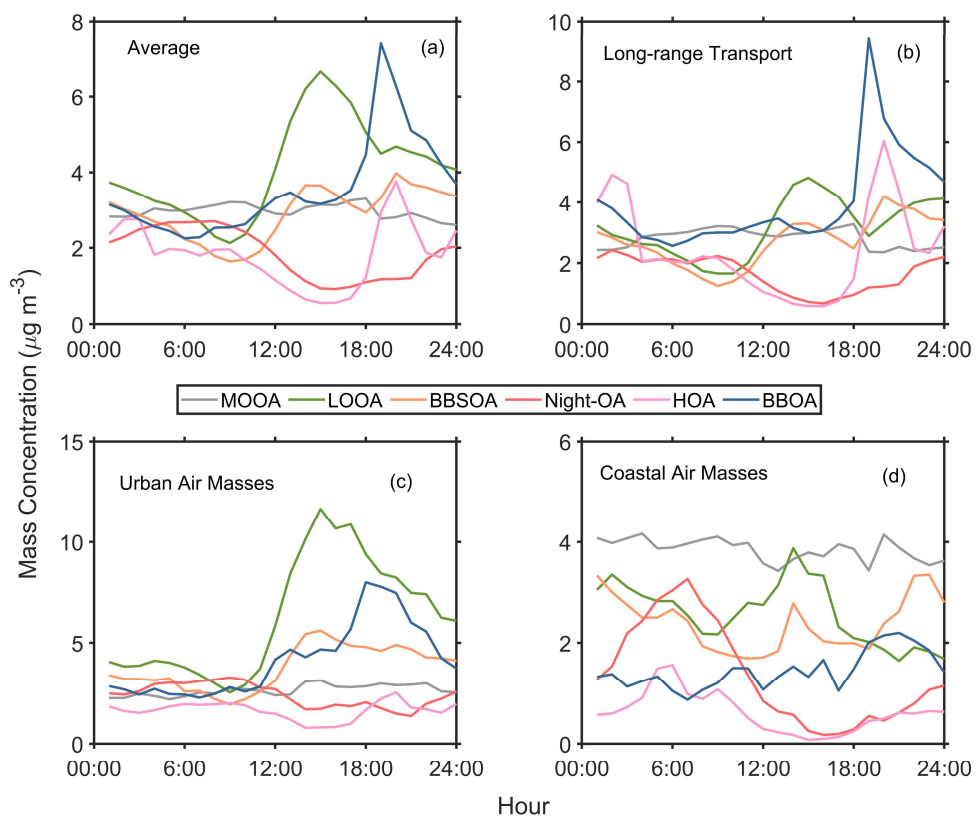
799



801

802 **Figure 1.** Temporal profile of the measured variables during the campaign. (a) particle number size
 803 distribution and condensation sink (black line); (b) one-dimensional thermograms of organic
 804 compounds (ions containing C, H, and O atoms, referred to as sum thermogram) and the T_{max}
 805 values (white dots) measured by the FIGAERO-CIMS; (c) bulk PM₁ chemical composition
 806 measured by SP-AMS and PM₁ concentration; (d) mass fraction of six OA factors from PMF
 807 analysis of SP-AMS data; (e) wind speed and wind direction. The color in (b) represents the
 808 normalized count per second (ncps) of oxygenated organic compounds calculated based on total
 809 count per second (cps) of oxygenated organic compounds at all m/z (*total cps*), m/z 127 (*cps*₁₂₇),
 810 and m/z 145 (*cps*₁₄₅) measured by FIGAERO-I-CIMS, $ncps = \frac{total\ cps}{(cps_{127} + cps_{145}) \cdot 10^6}$. The OA factors
 811 included more oxygenated OA (MOOA), less oxygenated OA (LOOA), aged biomass burning OA
 812 (BBSOA), hydrocarbon-like OA (HOA), biomass burning OA (BBOA), and nighttime OA (night-
 813 OA).

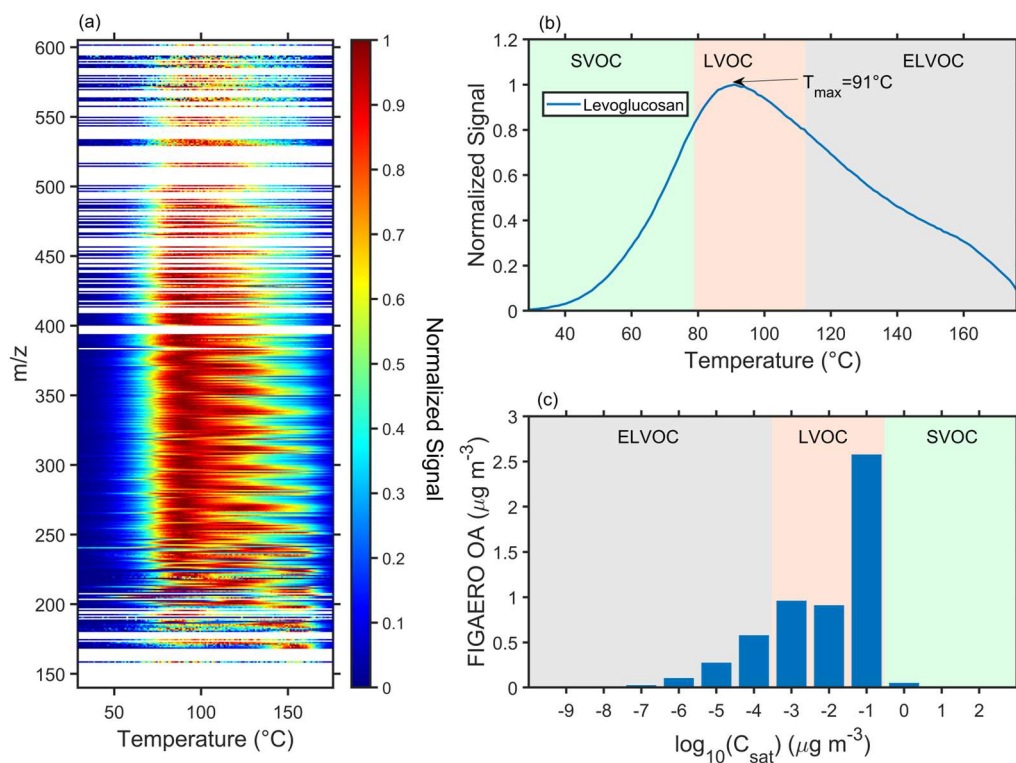
814



816

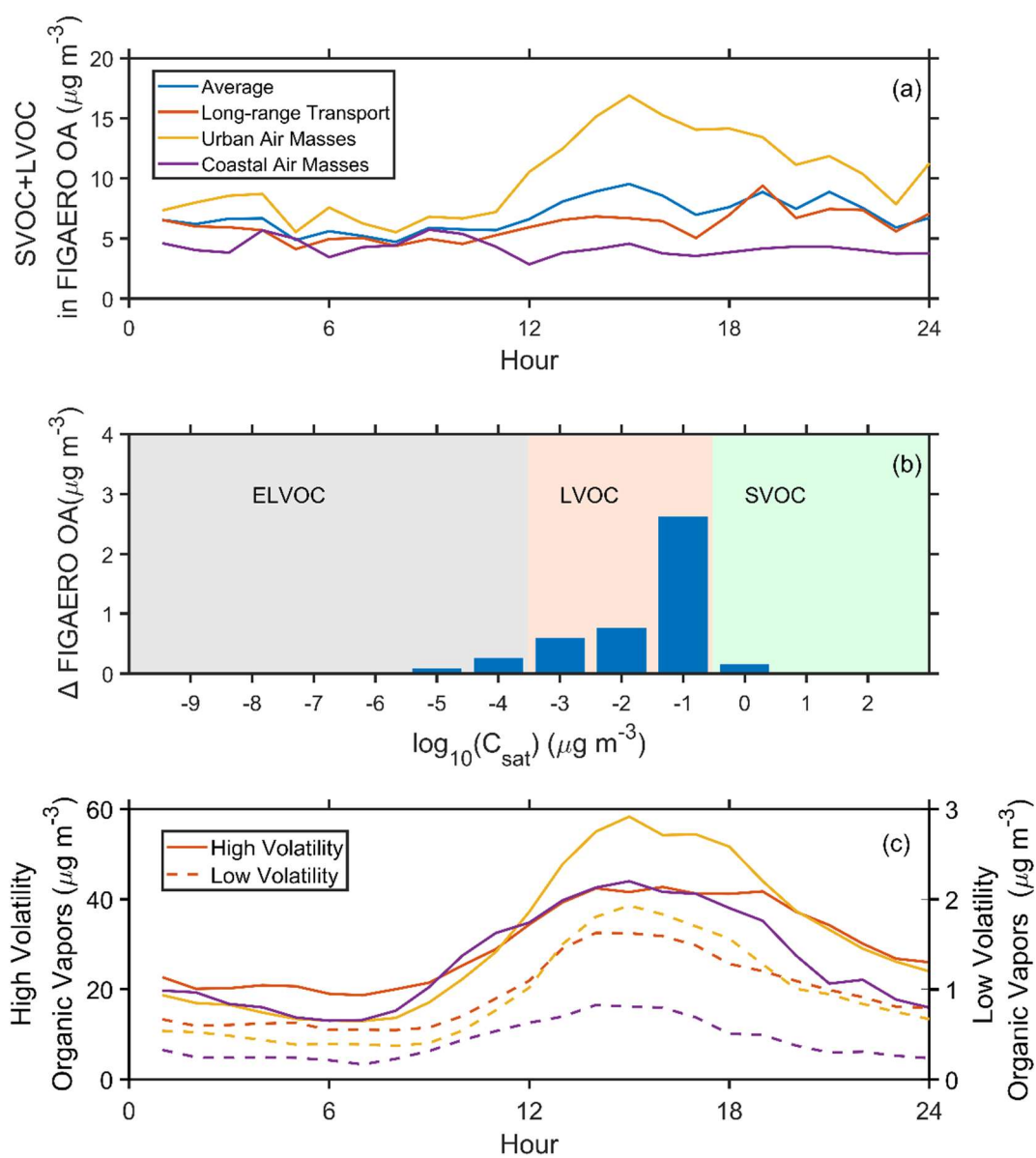
817 **Figure 2.** Average diurnal variation of six OA PMF factors during (a) the whole campaign, (b)

818 long-range transport, (c) urban air masses, and (d) coastal air masses periods.



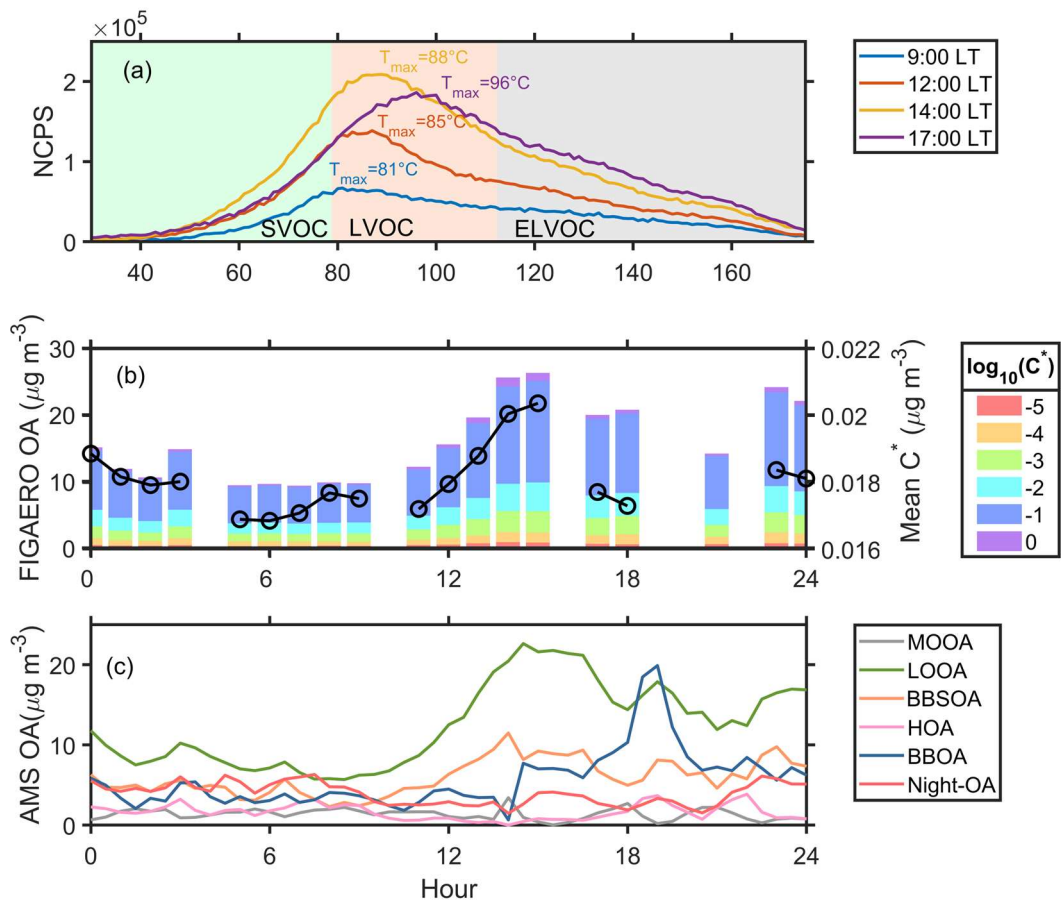
819

820 **Figure 3.** The average (a) two-dimensional thermograms of all calibrated and semi-quantified
 821 species, (b) one-dimensional thermogram of levoglucosan, and (c) volatility distribution of all
 822 calibration and semi-quantified species in the particle phase measured by the FIGAERO-CIMS
 823 (referred as FIGAERO OA). The T_{max} was converted to the C^* according to Eqs. (1) and (2).
 824



825

826 **Figure 4.** Diurnal variation of (a) SVOC+LVOC in FIGAERO OA, (b) the difference of
 827 FIGAERO OA between the urban air masses and long-range transport periods, and (c) low
 828 volatility organic vapors (ELVOC+LVOC, solid lines) and high volatility organic vapors
 829 (SVOC+LVOC+VOC, dash lines) during the whole campaign and three selected periods.



830

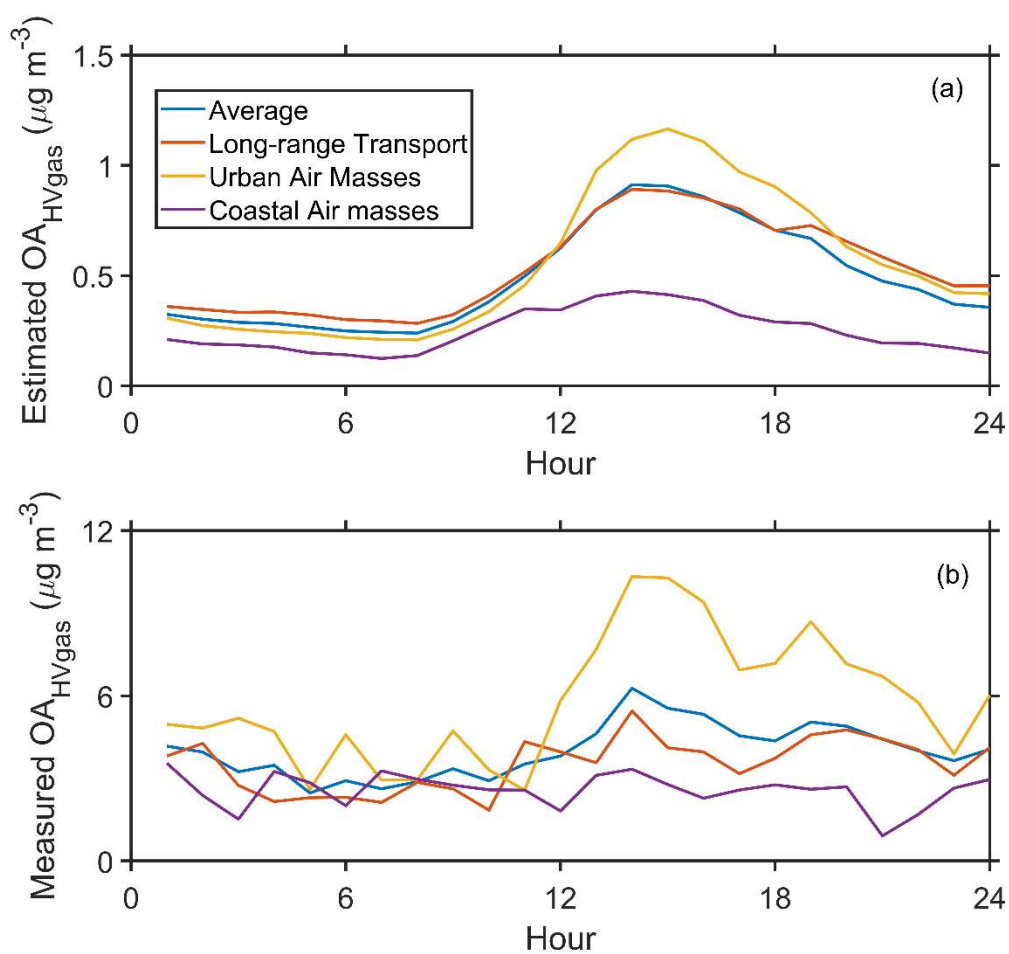
831 **Figure 5.** (a) The sum thermograms at 9:00, 12:00, 14:00, and 17:00, (b) variation of FIGAERO

832 OA volatility presented in a volatility range from 10^{-5} to $10^0 \mu\text{g m}^{-3}$ and mean C^* , and (c)

833 variation of six OA factors from PMF analysis on 2 November 2019. The mean $C^*(\bar{C}^*)$ is

834 estimated as $\bar{C}^* = 10^{\sum f_i \log_{10} C_i^*}$, where f_i is the mass fraction of OA with a volatility C_i^* .

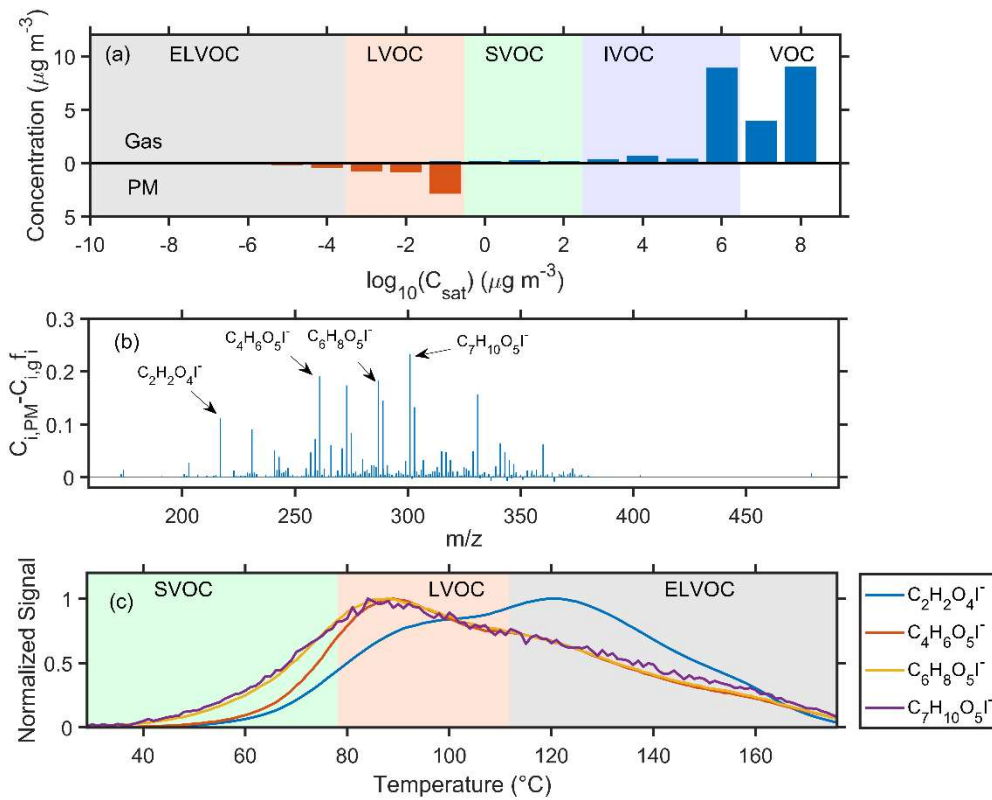
835



836

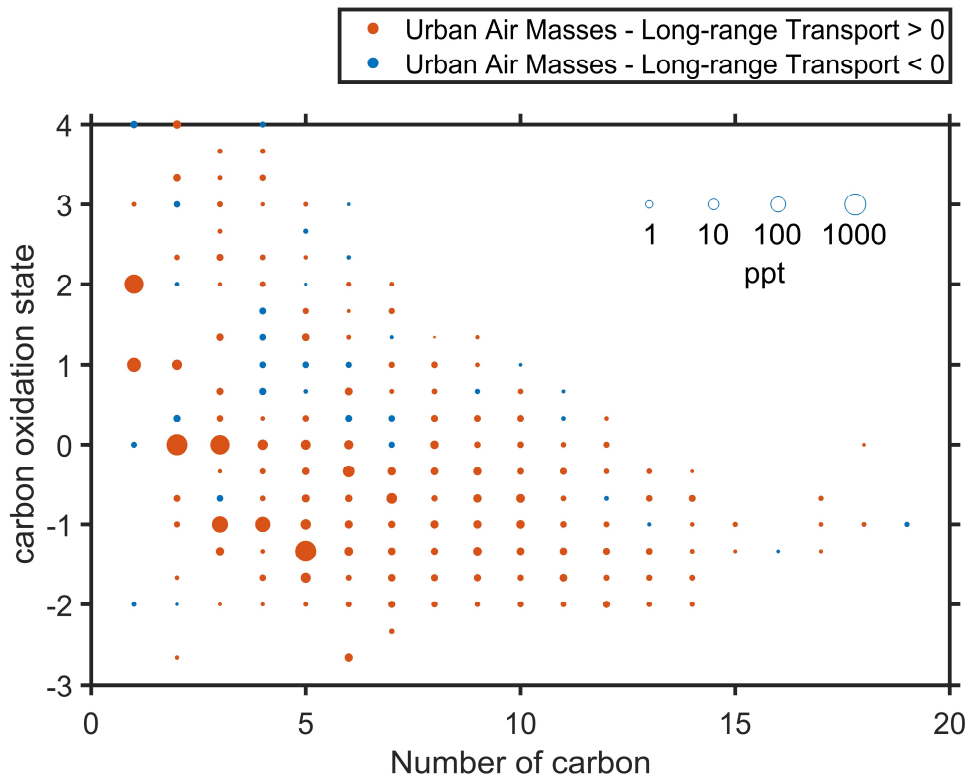
837 **Figure 6.** The diurnal variation of (a) the estimated contribution of high volatility organic vapors
 838 to the OA (Estimated OA_{HVgas}) and (b) the total concentration of corresponding species in the
 839 particles-phase measured by the FIGAERO CIMS.

840



841

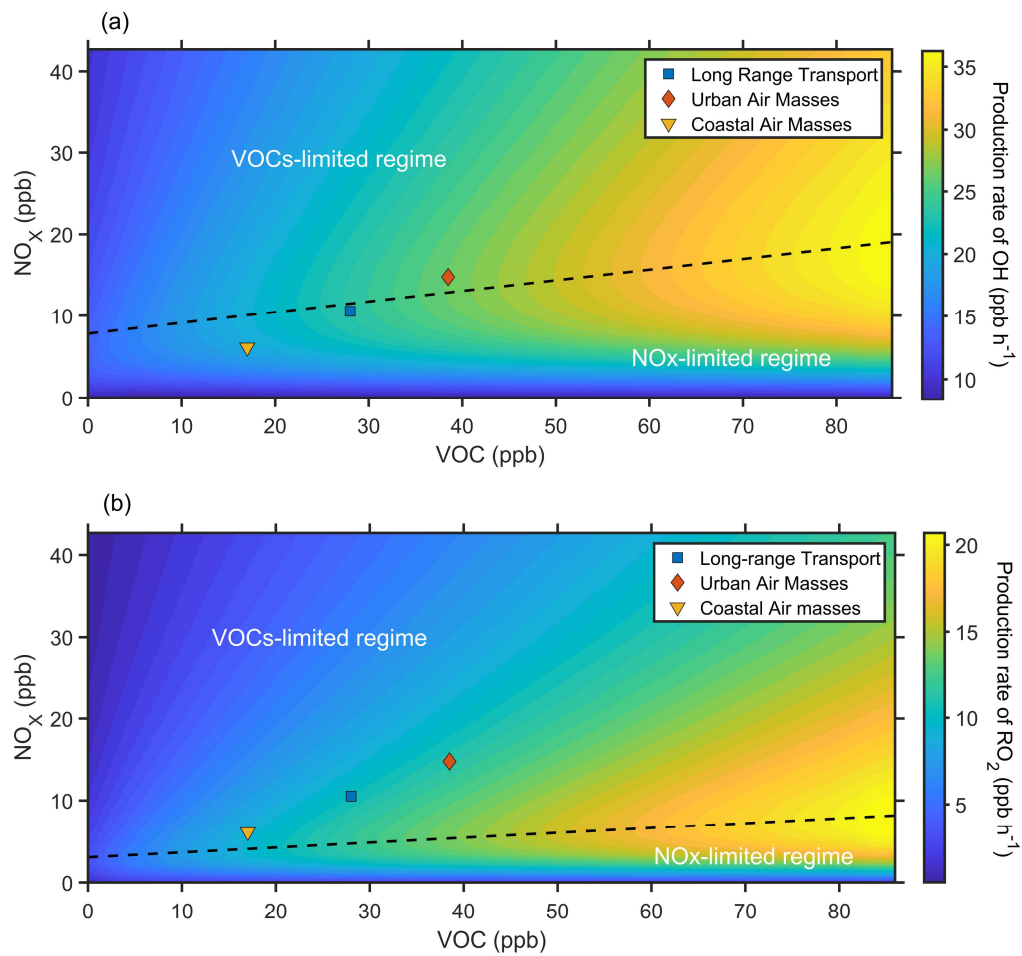
842 **Figure 7.** (a) The average volatility distribution of high volatility organic vapors in the gas-phase
 843 and particle-phase. (b) The average difference between the measured concentration in the particle-
 844 phase ($C_{i,PM}$) and the estimated concentration (C_{i,gf_i}) of different compounds in the high volatility
 845 organic vapors. (c) The average thermograms of $\text{C}_2\text{H}_2\text{O}_4\text{I}^-$, $\text{C}_4\text{H}_6\text{O}_5\text{I}^-$, $\text{C}_6\text{H}_8\text{O}_5\text{I}^-$, and $\text{C}_7\text{H}_{10}\text{O}_5\text{I}^-$.
 846



848

849 **Figure 8.** Difference in the carbon oxidation state ($\overline{OS_C}$) in the gas phase in the afternoon (12:00-
 850 16:00 LT) between the long-range transport and urban air masses periods. The symbol sizes are
 851 proportional to the logarithm of concentration. The symbol colors in a and b represent that the
 852 concentration during the urban air masses period was higher (red) or lower (blue) than that during
 853 the long-range transport period.

854



855

856 **Figure 9.** The simulated production rate of OH(a) and RO₂(b) with NO_x and VOCs concentration
 857 predicted by an observation-constrained box model under campaign average condition. Blue square,
 858 red diamond, and yellow triangle represent the average conditions during long-range transport,
 859 urban air masses, and coastal air masses period, respectively.

860